arXiv:1408.7084v2 [hep-ex] 9 Sep 2014

Measurement of Higgs boson production in the diphoton decay channel in pp collisions at center-of-mass energies of 7 and 8 TeV with the ATLAS detector

The ATLAS Collaboration

Abstract

A measurement of the production processes of the recently discovered Higgs boson is performed in the two-photon final state using 4.5 fb^{-1} of proton–proton collisions data at $\sqrt{s} = 7$ TeV and 20.3 fb^{-1} at $\sqrt{s} = 8$ TeV collected by the ATLAS detector at the Large Hadron Collider. The number of observed Higgs boson decays to diphotons divided by the corresponding Standard Model prediction, called the signal strength, is found to be $\mu = 1.17 \pm 0.27$ at the value of the Higgs boson mass measured by ATLAS, $m_H = 125.4$ GeV. The analysis is optimized to measure the signal strengths for individual Higgs boson production processes at this value of m_H. They are found to be $\mu_{\mathsf{ggF}} = 1.32 \pm 0.38$, $\mu_{\mathsf{VBF}} = 0.8 \pm 0.7$, $\mu_{WH} = 1.0 \pm 1.6$, $\mu_{ZH} = 0.1~^{+3.7}_{-0.1}$, and $\mu_{t\bar{t}H} = 1.6~^{+2.7}_{-1.8}$, for Higgs boson production through gluon fusion, vector-boson fusion, and in association with a W or Z boson or a top-quark pair, respectively. Compared with the previously published ATLAS analysis, the results reported here also benefit from a new energy calibration procedure for photons and the subsequent reduction of the systematic uncertainty on the diphoton mass resolution. No significant deviations from the predictions of the Standard Model are found.

Measurement of Higgs boson production in the diphoton decay channel in pp collisions at center-of-mass energies of 7 and 8 TeV with the ATLAS detector

A measurement of the production processes of the recently discovered Higgs boson is performed in the two-photon final state using 4.5 fb^{-1} of proton–proton collisions data at $\sqrt{s} = 7$ TeV and 20.3 fb^{-1} at $\sqrt{s} = 8$ TeV collected by the ATLAS detector at the Large Hadron Collider. The number of observed Higgs boson decays to diphotons divided by the corresponding Standard Model prediction, called the signal strength, is found to be $\mu = 1.17 \pm 0.27$ at the value of the Higgs boson mass measured by ATLAS, $m_H = 125.4$ GeV. The analysis is optimized to measure the signal strengths for individual Higgs boson production processes at this value of m_H. They are found to be $\mu_{\text{ggF}} = 1.32 \pm 0.38$, $\mu_{\text{VBF}} = 0.8 \pm 0.7$, $\mu_{WH} = 1.0 \pm 1.6$, $\mu_{ZH} = 0.1\,^{+3.7}_{-0.1}$, and $\mu_{t\bar{t}H} = 1.6\,^{+2.7}_{-1.8}$, for Higgs boson production through gluon fusion, vector-boson fusion, and in association with a W or Z boson or a top-quark pair, respectively. Compared with the previously published ATLAS analysis, the results reported here also benefit from a new energy calibration procedure for photons and the subsequent reduction of the systematic uncertainty on the diphoton mass resolution. No significant deviations from the predictions of the Standard Model are found.

I. INTRODUCTION

In July 2012, the ATLAS and CMS collaborations independently reported observations of a new particle [1, 2] compatible with the Standard Model (SM) Higgs boson [3–8]. Since then, measurements of the properties of this new boson have been carried out to further elucidate its role in electroweak symmetry breaking and the mechanism of fermion mass generation. In addition to measurements of its mass [9, 10] and its spin and parity [11, 12], the strengths of the couplings of the Higgs boson to fermions and vector bosons are of primary interest [10, 13]. These couplings, which are predicted to depend on the value of m_H, can be tested by measurements of the ratios of the number of observed Higgs bosons produced through gluon fusion (ggF), weak vector-boson fusion (VBF) and associated production with a W boson (WH), a Z boson (ZH) or a top-quark pair ($t\bar{t}H$) to the corresponding SM predictions. The good diphoton invariant mass resolution of the ATLAS detector makes it possible to measure these ratios, or *signal strengths* μ, in the diphoton final state, separating the small, narrow Higgs boson signal from the large continuum background.

Measurements of the individual signal strengths of the production processes listed above are presented in this article. They probe both the Higgs boson production and the $H \to \gamma\gamma$ decay rate: in order to test the production through VBF and associated production with a W or Z boson or a $t\bar{t}$ pair independently of the $H \to \gamma\gamma$ branching ratio, signal strengths of these processes relative to ggF production are also presented. A combination of 4.5 fb^{-1} of pp collision data recorded at $\sqrt{s} = 7$ TeV and 20.3 fb^{-1} of data recorded at $\sqrt{s} = 8$ TeV (the LHC Run 1 data) is analyzed. The analysis is designed to maximize the sensitivity to the signal strengths while using the same event selection as the measurement of the Higgs boson mass discussed in Ref. [9]. This is achieved by defining categories of diphoton candidate events that exploit the characteristic features of the final states of the different production modes.

The signal strengths are extracted from maximum likelihood fits to unbinned invariant mass distributions of diphoton candidates observed in the different event categories, modeled by a narrow Higgs boson resonance on continuum backgrounds. All the results presented in this article are obtained for a Higgs boson mass $m_H = 125.4$ GeV measured by ATLAS using the combination of results from the decay channels $H \to \gamma\gamma$ and $H \to ZZ^{(*)} \to 4\ell$ [9]. The CMS collaboration has recently updated its measurements of the Higgs properties in the diphoton channel as discussed in Ref. [14].

Compared with the previous results obtained with the same dataset [13], this new analysis profits from a refined energy calibration procedure that improves the expected mass resolution of the signal in the inclusive diphoton sample by approximately 10% [15]. In addition, the uncertainty on the photon energy resolution is reduced by approximately a factor of two. Furthermore, experimental uncertainties on the integrated luminosity, photon identification, and photon isolation are reduced. Two new categories enriched in $t\bar{t}H$ events and a dedicated dilepton category that distinguishes ZH from WH production have been added. Finally, the event selection and categorization are tuned to improve the sensitivity of the analysis. The above refinements contribute almost equally to an overall improvement of about 10% in the expected uncertainty on the combined signal strength.

The article is organized in the following way. The ATLAS detector is briefly described in Sec. II. The data and Monte Carlo (MC) samples used for this analysis are presented in Sec. III while details of the reconstruction of photons, electrons, muons, jets and missing transverse momentum are given in Sec. IV. The diphoton event selection is discussed in Sec. V followed by a description of the event categorization in Sec. VI. The models of the signal and background distributions used to fit the data are presented in Sec. VII. The systematic uncertainties are described in Sec. VIII. Using the statistical procedure briefly outlined in Sec. IX, the results of the combination of the $\sqrt{s} = 7$ TeV and $\sqrt{s} = 8$ TeV data for the Higgs boson signal strengths are extracted and presented in Sec. X. The conclusions of this study are summarized

in Sec. XI.

II. THE ATLAS DETECTOR

The ATLAS experiment [16] is a multipurpose particle physics detector with a forward-backward symmetric cylindrical geometry and nearly 4π coverage in solid angle.[1]

The inner tracking detector (ID) covers the pseudorapidity range $|\eta| < 2.5$ and consists of a silicon pixel detector, a silicon microstrip detector, and a transition radiation tracker (TRT) in the range $|\eta| < 2.0$. The ID is surrounded by a superconducting solenoid providing a 2 T magnetic field. The ID allows an accurate reconstruction of charged-particle tracks originating from the proton–proton collision region as well as from secondary vertices, which permits an efficient reconstruction of photons interacting in the ID through e^+e^- pair production up to a radius in the transverse plane of about 80 cm.

The electromagnetic (EM) calorimeter is a lead/liquid-argon (LAr) sampling calorimeter with an accordion geometry. It is divided into two barrel sections that cover the pseudorapidity region $|\eta| < 1.475$ and two end-cap sections that cover the pseudorapidity regions $1.375 < |\eta| < 3.2$. It consists of three (two) longitudinal layers in shower depth in the region $|\eta| < 2.5$ $(2.5 < |\eta| < 3.2)$. The first one has a thickness of approximately four radiation lengths and, in the ranges $|\eta| < 1.4$ and $1.5 < |\eta| < 2.4$, is segmented into high-granularity strips in the η direction, typically 0.003×0.1 in $\eta \times \phi$ in the barrel regions. The first-layer sampling strips provide event-by-event discrimination between prompt photon showers and two overlapping showers coming from a $\pi^0 \to \gamma\gamma$ decay. The second layer, which collects most of the energy deposited in the calorimeter by photons and electrons, has a thickness of about 17 radiation lengths and a granularity of 0.025×0.025 in $\eta \times \phi$. The third layer, which has a thickness ranging from two to twelve radiation lengths as a function of η, is used to account for longitudinal fluctuations of high-energy electromagnetic showers. A thin presampler layer located in front of the EM calorimeter in the pseudorapidity interval $|\eta| < 1.8$ is used to correct for energy loss upstream of the calorimeter.

The hadronic calorimeter, which surrounds the EM calorimeter, consists of a steel/scintillator-tile calorimeter in the range $|\eta| < 1.7$ and two copper/LAr calorime-

ters spanning $1.5 < |\eta| < 3.2$. The acceptance is extended to $|\eta| = 4.9$ by two sampling calorimeters longitudinally segmented in shower depth into three sections using LAr as active material and copper (first section) or tungsten (second and third sections) as absorber.

The muon spectrometer (MS), located outside the calorimeters, consists of three large air-core superconducting toroid systems with precision tracking chambers that provide accurate muon tracking for $|\eta| < 2.7$ and fast detectors for triggering for $|\eta| < 2.4$.

A three-level trigger system is used to select events containing two photon candidates. The first-level trigger is hardware-based: using a cell granularity (0.1×0.1 in $\eta \times \phi$) that is coarser than that of the EM calorimeter, it searches for electromagnetic deposits with a transverse energy E_{T} above a programmable threshold. The second- and third-level triggers (collectively referred to as the *high-level trigger*) are implemented in software and exploit the full granularity and accurate energy calibration of the calorimeter.

III. DATA AND MONTE CARLO SAMPLES

Events from pp collisions were recorded using a diphoton trigger with E_{T} thresholds of 35 GeV and 25 GeV for the leading and sub-leading photon candidates, respectively, in the 8 TeV data and 20 GeV for both photon candidates in the 7 TeV data [17]. In the high-level trigger, clusters of energy in the EM calorimeter were reconstructed and required to satisfy loose criteria according to expectations for EM showers initiated by photons. This trigger has a signal efficiency above 99% for events fulfilling the final event selection. After application of data quality requirements, the 8 TeV (7 TeV) data sample corresponds to a total integrated luminosity of 20.3 fb^{-1} (4.5 fb^{-1}). The instantaneous luminosity is typically about $6 \cdot 10^{33}$ cm^{-2} s^{-1} ($3 \cdot 10^{33}$ cm^{-2} s^{-1}) in the analyzed 8 TeV (7 TeV) data, resulting in an average number of pp collisions per bunch crossing of about 21 (9) in the 8 TeV (7 TeV) data.

Simulated samples of Higgs bosons decaying into two photons were generated separately for the five production modes whose signal strengths are measured here (ggF, VBF, WH, ZH, and $t\bar{t}H$) and for Higgs boson masses from 100 GeV to 160 GeV (115 GeV to 135 GeV for the $t\bar{t}H$ samples) in 5 GeV steps. Samples of Higgs boson events produced in association with a single top quark, tH, which is predicted to make a small contribution to the selection of candidates from $t\bar{t}H$ production, were also generated.

The AU2 [18] tuning of PYTHIA8 [19] is used to simulate the minimum-bias events and the underlying event. The normalizations of the production mode samples are performed following the recommendations of the LHC Higgs cross-section working group [20] as described below.

Gluon fusion events are generated with POWHEG-

---

[1] ATLAS uses a right-handed coordinate system with its origin at the nominal interaction point (IP) in the center of the detector and the z-axis along the beam pipe. The x-axis points from the IP to the center of the LHC ring, and the y-axis points upward. Cylindrical coordinates (r, ϕ) are used in the transverse plane, ϕ being the azimuthal angle around the beam pipe. The pseudorapidity is defined in terms of the polar θ angle as $\eta = -\ln[\tan(\theta/2)]$.

BOX [21–25] interfaced with PYTHIA8 for the underlying event, parton showering and hadronization. The overall normalization of the ggF process used to estimate the expected event rate is taken from a calculation at next-to-next-to-leading order (NNLO) [26–31] in QCD. Next-to-leading-order (NLO) electroweak (EW) corrections are also included [32, 33]. The effect of the interference of $gg \to H \to \gamma\gamma$ with the continuum $gg \to \gamma\gamma$ background induced by quark loops is taken into account using an averaging procedure [34] that combines LO [35] and NLO corrections [36]: the destructive interference causes a $\sim 1\%$ reduction of the ggF cross section.

The VBF samples are generated using POWHEG-BOX [37] interfaced with PYTHIA8 and normalized to a cross section calculated with full NLO QCD and EW corrections [38–40] with an approximate NNLO QCD correction applied [41].

Higgs bosons produced in association with a Z boson or a W boson (collectively referred to as VH) are generated with PYTHIA8. The predictions for VH are normalized to cross sections calculated at NNLO [42] with NLO EW radiative corrections [43] applied.

The $t\bar{t}H$ samples are generated using the POWHEL generator, a combination of the POWHEG-BOX and HELAC-NLO [44] generators, interfaced with PYTHIA8. The full NLO QCD corrections are included [45–48] in the $t\bar{t}H$ normalization. A sample of events from tH production in the t-channel in association with a b-jet and a light jet j ($tHbj$) are generated with MADGRAPH [49] interfaced with PYTHIA8; the normalization of the production cross section is taken from Refs. [50–54]. A sample of tH events produced in association with a W boson (tHW) is generated using MADGRAPH5_AMC@NLO [55] interfaced to HERWIG++ [56].

The branching ratio for $H \to \gamma\gamma$ and its uncertainty [57, 58] are compiled in Ref. [20]. The CT10 [59] parton distribution function (PDF) set is used for the POWHEG-BOX samples while CTEQ6L1 [60] is used for the PYTHIA8 samples.

Additional corrections to the shape of the generated p_T distribution of Higgs bosons produced by gluon fusion are applied to match the distribution from a calculation at NNLO+NNLL provided by HRES2.1, which includes exact calculations of the effects of the top and bottom quark masses [61, 62] as well as dynamical renormalization and factorization scales. Calculations based on HRES predict a lower rate of events at high p_T compared with the nominal POWHEG-BOX samples and thus the contribution from events with two or more jets, which mostly populate the high-p_T region, is affected. To simultaneously reproduce the inclusive Higgs p_T distribution as well as the ≥ 2 jet component, the ggF events with two or more jets are first normalized to a NLO calculation [63]. Then, Higgs boson p_T-dependent weighting functions are determined using an iterative procedure. First, the events with two or more jets are weighted in order to match the Higgs boson p_T distribution from MINLO HJJ predictions [64]. As a second step, the inclusive spectrum

is weighted to match the HRES distribution. These two steps are iteratively repeated until the inclusive Higgs p_T spectrum agrees well with the HRES prediction while preserving the normalization of the ≥ 2 jet component. The events simulated for VBF, WH, and ZH production are re-weighted so that the p_T distributions of the Higgs bosons match the ones predicted by HAWK [65–67].

The contribution from Higgs boson production in association with a $b\bar{b}$ pair ($b\bar{b}H$) is accounted for in this analysis: the cross section of this process is calculated in a four-flavor PDF scheme (4FS) at NLO QCD [68–70] and a five-flavor PDF scheme (5FS) at NNLO QCD [71]. These two calculations are combined using the Santander matching procedure [72, 73]. Since the p_T spectrum of the b-jets is expected to be soft, the jet environments for ggF and $b\bar{b}H$ production are quite similar and thus the detection efficiency for $b\bar{b}H$ is assumed to be the same as for ggF.

The invariant mass distributions and normalizations of the backgrounds in the event categories are estimated by fits to the data. However, the choices of the functional forms used to model the backgrounds and the uncertainties associated with these choices are determined mostly by MC studies, as described in detail in Sec. VII B. For these studies $\gamma\gamma$ and γ–jet background samples were generated by SHERPA [74, 75] and the jet–jet background samples by PYTHIA8. The normalizations of these samples are determined by measurements of a data sample of preselected diphoton events as described in Sec. VII B. More details about the background control sample used for each category are also given in Sec. VII B.

A summary of the event generators and PDF sets for the individual signal and background processes used in this analysis is reported in Table I. The normalization accuracy and SM cross sections with $m_H = 125.4$ GeV for $\sqrt{s} = 7$ TeV and $\sqrt{s} = 8$ TeV are also given for the different Higgs production modes.

The stable particles, defined as the particles with a lifetime longer than 10 ps, are passed through a full detector simulation [76] based on GEANT4 [77]. Pileup effects are simulated by overlaying each MC event with a variable number of MC inelastic pp collisions generated using PYTHIA8, taking into account in-time pileup (collisions in the same bunch crossing as the signal), out-of-time pileup (collisions in other bunch crossings within the time-window of the detector sensitivity), and the LHC bunch train structure. The MC events are weighted to reproduce the distribution of the average number of interactions per bunch crossing observed in the data. The resulting detector signals are passed through the same event reconstruction algorithms as used for the data. Since the length of the beam spot along the beam axis is slightly wider in the MC samples than in the data, a weighting procedure is applied to the 8 TeV (7 TeV) MC events to match the 4.8 cm (5.6 cm) RMS length observed in the 8 TeV (7 TeV) data.

In order to increase the number of available MC background events, especially for the optimization of the event

TABLE I. Summary of event generators and PDF sets used to model the signal and the main background processes. The SM cross sections σ for the Higgs production processes with $m_H = 125.4$ GeV are also given separately for $\sqrt{s} = 7$ TeV and $\sqrt{s} = 8$ TeV, together with the orders of the calculations.

Process	Generator	Showering	PDF set	Order of calculation	σ[pb] $\sqrt{s} = 7$ TeV	σ[pb] $\sqrt{s} = 8$ TeV
ggF	Powheg-box	Pythia8	CT10	NNLO(QCD)+NLO(EW)	15.04	19.15
VBF	Powheg-box	Pythia8	CT10	NLO(QCD+EW)+app.NNLO(QCD)	1.22	1.57
WH	Pythia8	Pythia8	CTEQ6L1	NNLO(QCD)+NLO(EW)	0.57	0.70
ZH	Pythia8	Pythia8	CTEQ6L1	NNLO(QCD)+NLO(EW)	0.33	0.41
$t\bar{t}H$	Powhel	Pythia8	CT10	NLO(QCD)	0.09	0.13
$tHbj$	MadGraph	pythia8	CT10	NLO(QCD)	0.01	0.02
tHW	MadGraph5_aMC@NLO	herwig++	CT10	NLO(QCD)	<0.01	<0.01
$b\bar{b}H$	-	-	-	5FS(NNLO)+4FS(NLO)	0.15	0.20
$\gamma\gamma$	Sherpa	Sherpa	CT10			
γ–jet	Sherpa	Sherpa	CT10			
jet–jet	Pythia8	Pythia8	CTEQ6L1			

categorization (Sec. VI) and background shape parameterization studies (Sec. VII B), MC samples based on fast, simplified models of the detector response rather than full simulation are used: the resolutions and reconstruction efficiencies for photons and jets are tuned as functions of the transverse momentum and pseudorapidity to reproduce the ones obtained from fully simulated samples of $\gamma\gamma$ and γ–jet events. These samples are typically about 1000 times larger than the corresponding collected data samples after analysis selections.

IV. PHYSICS OBJECT DEFINITIONS

The reconstruction and identification of the physics objects (photons, electrons, muons, jets) and the measurement of missing transverse momentum are described here. Unless otherwise stated, the descriptions apply to both the 7 TeV and the 8 TeV data.

A. Photons

The photon reconstruction is seeded by energy deposits (clusters) in the EM calorimeter with $E_T > 2.5$ GeV in projective towers of size 0.075×0.125 in the $\eta \times \phi$ plane. The reconstruction algorithm looks for possible matches between energy clusters and tracks reconstructed in the inner detector and extrapolated to the calorimeter. Well-reconstructed tracks matched to clusters are classified as electron candidates while clusters without matching tracks are classified as unconverted photon candidates. Clusters matched to pairs of tracks that are consistent with the hypothesis of a $\gamma \to e^+e^-$ conversion process are classified as converted photon candidates. Due to the intrinsic ambiguity between electron and photon signatures, clusters may be reconstructed both with electron and photon hypotheses to maximize the reconstruc-

tion efficiency for both. In particular, clusters matched to single tracks without hits in an active region of the pixel layer nearest to the beam pipe are considered both as converted photon candidates [78] and electron candidates. The cluster reconstruction efficiency for photons with $E_T > 25$ GeV is estimated from simulation [78] to be close to 100% while the efficiency to actually reconstruct them as photons is 96%. In the remaining cases these clusters are incorrectly reconstructed as electrons but not as photons. The probability for a real electron with $E_T > 25$ GeV to be reconstructed as a photon fulfilling the tight identification criteria described below is measured in data to vary between 3% and 10%, depending on the pseudorapidity and the conversion class of the candidate.

In the following, a brief review of the calibration procedure for photons is reported; a detailed description can be found in Ref. [15]. The energy measurement is performed by summing the energies measured in the EM calorimeter cells belonging to the candidate cluster. The size of the cluster depends on the photon classification: in the barrel, a $\Delta\eta \times \Delta\phi = 0.075 \times 0.125$ cluster is used for unconverted photons and 0.075×0.175 for converted photons to account for the opening of the e^+e^- pair in the ϕ direction due to the magnetic field. In the endcap, a cluster size of $\Delta\eta \times \Delta\phi = 0.125 \times 0.125$ is used for all candidates. The cluster energy has to be corrected for energy losses in the inactive materials in front of the calorimeter, for the fraction of energy deposited outside the area of the cluster in the $\eta\phi$-plane and into the hadronic calorimeter in the direction of the shower propagation. Finally, due to the finite cluster size in η and ϕ coordinates and the variation of the amount of absorber material crossed by incident particles as a function of ϕ, a correction has to account for the variation of the energy response as a function of the impact point on the calorimeter. The calibration coefficients used to make this correction are obtained from a detailed simu-

lation of the detector geometry and are optimized with a boosted decision tree (BDT) [79]. The response is calibrated separately for converted and unconverted photon candidates. The inputs to the energy calibration algorithm are the measured energy per calorimeter layer, including the presampler, the η position of the cluster and the local position of the shower within the second-layer cell corresponding to the cluster centroid. In addition, the track transverse momenta and the conversion radius for converted photons are used as input to the regression algorithm to further improve the energy resolution, especially at low energy. This new calibration procedure gives a 10% improvement in the expected invariant mass resolution for $H \to \gamma\gamma$ events with respect to the calibration used in our previous publications. The energy scales of the data and simulation are equalized by applying η-dependent correction factors to match the invariant mass distributions of $Z \to ee$ events. In this procedure, the simulated width of the Z boson resonance is matched to the one observed in data by adding a contribution to the constant term of the electron energy resolution. The photon energy scale uncertainty is 0.2–0.3% for $|\eta| < 1.37$ and $|\eta| > 1.82$, and 0.6% for $1.52 < |\eta| < 1.82$. A similar accuracy is achieved for converted and unconverted photons, and the energy dependence of the uncertainty is weak. The uncertainties in the photon energy scales are confirmed by an independent analysis of radiative Z boson decays. The relative uncertainty on the energy resolution is about 10% for photons with $E_{\mathrm{T}} \sim 60$ GeV. The uncertainty on the photon energy resolution is reduced by approximately a factor of two with respect to our previous publications: this reduction comes from improvements on the detector simulation model, from a better knowledge of the material upstream of the calorimeter, and from more detailed calibration corrections applied to the data [15]. These improvements lead to a better agreement between the m_{ee} distributions in simulated $Z \to ee$ events with the ones measured in data, that in turn prompt a reduced uncertainty of the energy resolution effective constant term. In addition, the new procedure to compute the photon energy resolution uncertainty is more effective at disentangling the contributions from the knowledge of the material in front of the calorimeter and of the intrinsic calorimeter energy resolution, as discussed in Sec. VIII C 1. The energy response of the calorimeter in data varies by less than 0.1% over time. The simulation is found to describe the dependence of the response on pileup conditions at the same accuracy level.

The photon identification algorithm is based on the lateral and longitudinal energy profiles of the shower measured in the calorimeter [80]. First, the fraction of energy in the hadronic calorimeter is used, together with the shape of the lateral profile of the shower as measured in the second layer of the electromagnetic calorimeter, to reject photon candidates from jets with a large hadronic component. Then, observables built from measurements in the high-granularity first layer of the calorimeter are used to discriminate prompt photons from overlapping photon pairs that originate in the decays of neutral mesons produced in jet fragmentation. Based on these discriminating variables, two sets of tight identification criteria, for converted and unconverted photon candidates, are applied to the 8 TeV data. The identification criteria are based on rectangular cuts optimized on simulated electromagnetic showers in γ–jet events and simulated jets in QCD dijet events. The agreement between data and simulation for the individual discriminating variables is checked using a pure sample of photons from radiative $Z \to \ell\ell\gamma$ decays (where ℓ is an electron or a muon) and an inclusive photon sample after background subtraction. As a result, small corrections are applied to the identification variables in the simulation to account for the observed mis-modeling of lateral shower profiles in the calorimeter. The photon identification cuts are carefully tuned to guarantee stability of the efficiency as a function of the in-time pileup within a few per cent. The identification efficiency for unconverted (converted) photons is typically 83–95% (87–99%) for $30 < E_{\mathrm{T}} < 100$ GeV. Correction factors as a function of η, E_{T} and conversion class are derived to correct for the residual mismatch between the efficiency in the simulation and the efficiency measured in the data. For the analysis of the 7 TeV data, the discriminating observables are combined into a single discriminant by a neural-network (NN) algorithm [79]: with similar jet rejection power, the multivariate approach improves the identification efficiency by 8–10% with respect to the cut-based identification [80]. For the analysis of the 8 TeV data, the re-optimized cut-based identification has a similar jet rejection power for a given identification efficiency.

Two complementary isolation variables are used to further suppress the number of jets in the photon candidate samples. The first variable is the sum of the transverse energies of positive-energy topological clusters [81] deposited in the calorimeter within a cone of $\Delta R \equiv \sqrt{(\Delta\eta)^2 + (\Delta\phi)^2} = 0.4$ around each photon. The energy sum excludes the contribution due to the photon cluster and an estimate of the energy deposited by the photon outside its associated cluster. The median E_{T} density for the event in question, caused by the underlying event (UE) and additional minimum-bias interactions occurring in the same or neighboring bunch crossings (in-time and out-of-time pileup, respectively), is subtracted on an event-by-event basis using an algorithm described in Ref. [82] and implemented as described in Ref. [83]. Despite these corrections, a residual dependence of the calorimetric isolation selection efficiency ϵ_{iso} on the number of primary vertices reconstructed by the inner tracking detector [84] is observed: an example is shown in Fig. 1 for a maximum allowed energy of 4 GeV in the isolation cone. To improve the efficiency of the isolation selection for events with large pileup, the calorimetric isolation is complemented by a track isolation defined as the scalar sum of the transverse momenta of all tracks with $p_{\mathrm{T}} > 1$ GeV (0.4 GeV for the 7 TeV data) within a cone

of size $\Delta R = 0.2$ around each photon. The track isolation efficiency is insensitive to out-of-time pileup and its dependence on the in-time pileup is reduced by selecting only tracks consistent with originating from the diphoton production vertex (defined in Sec. V) and not associated with converted photon candidates. A track in the 7 TeV (8 TeV) data is considered to be associated with the diphoton production vertex if the point of closest approach of its extrapolation is within 5 mm (15 mm) of the vertex along the z-axis and within 0.5 mm (1.5 mm) of the vertex in the transverse plane. For a given sample purity, a reduction of the dependence of the selection efficiency on the in-time pileup is obtained by combining a looser calorimeter isolation selection with a track isolation requirement. Photon candidates are required to have a calorimetric isolation less than 6 GeV (5.5 GeV for the 7 TeV data) and a track isolation less than 2.6 GeV (2.2 GeV for the 7 TeV data). The efficiency of the isolation cuts in the simulation is corrected by a small p_{T}-dependent factor extracted from measurements in data performed with a pure sample of photons from radiative $Z \to ee\gamma$ decays and $Z \to ee$ events.
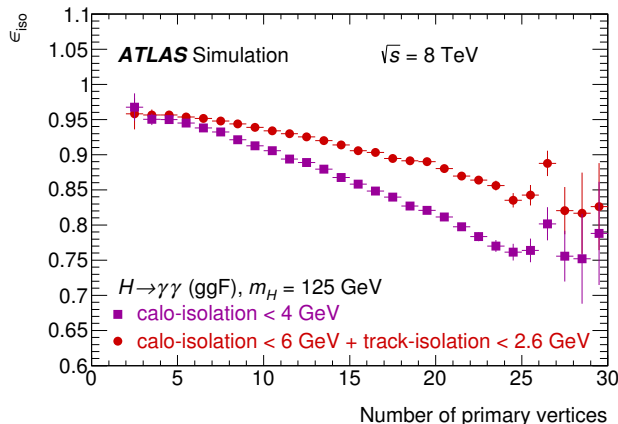

FIG. 1. Efficiency ϵ_{iso} to fulfill the isolation requirement as a function of the number of primary vertices in each event, determined with a MC sample of Higgs bosons decaying into two photons with m_H=125 GeV and $\sqrt{s} = 8$ TeV. Events are required to satisfy the kinematic selection described in Sec. V. The efficiency of the event selection obtained with a tight calorimetric isolation requirement (4 GeV) is compared with the case in which a looser calorimetric isolation (6 GeV) is combined with a track isolation (2.6 GeV) selection.

B. Leptons

Electron candidates, as mentioned above, are built from clusters of energy deposited in the electromagnetic calorimeter that are associated with at least one well-reconstructed track in the inner detector. In this analysis electron candidates are required to satisfy the loose identification criterion of a likelihood-based discriminat-

ing variable [85]. A cut-based identification selection is used in the 7 TeV analysis and the electrons are required to fulfill the medium criteria defined in Ref. [86]. The determination of the energy of the electron candidate is performed using a $\Delta\eta \times \Delta\phi = 0.075 \times 0.175$ cluster in the barrel to recover the energy spread in ϕ from bremsstrahlung photons while a 0.125×0.125 cluster is used in the end-cap. The cluster energy is calibrated as discussed in Sec. IV A with a dedicated set of calibration coefficients optimized for electrons. The transverse momentum p_{T} of an electron is computed from the cluster energy and the track direction at the interaction point. Electrons are required to be in the region $|\eta| < 2.47$ and to satisfy $E_{\mathrm{T}} > 15$ GeV. Finally, the electron candidates must satisfy both the track-based and calorimetric isolation criteria relative to the E_{T} of the candidate. The calorimetric transverse isolation energy within a $\Delta R = 0.4$ cone is required to be less than 20% of the electron candidate's E_{T}, whereas the sum of the transverse momenta of the tracks within a cone of $\Delta R = 0.2$ around the track of the electron candidate is required to be less than 15% of the electron candidate's E_{T}.

Muon candidates are formed from tracks reconstructed independently in the MS and in the ID and from energy deposits measured in the calorimeters [87]. Different types of muon candidates are built depending on the available information from the different sub-detector systems: the main algorithm combines tracks reconstructed separately by the ID and the MS. To extend the acceptance region beyond the ID limit to include $2.5 < |\eta| < 2.7$, tracks reconstructed in the MS stand-alone are used. Finally, to increase the acceptance for low-p_{T} muons or for muons that pass through uninstrumented regions of the MS, muon candidates are reconstructed from tracks in the ID associated with a track segment in the MS or to a calorimetric energy deposition compatible with the one from a minimum-ionizing particle. In this analysis, muons from all different algorithms are used and required to have $|\eta| < 2.7$ and $p_{\mathrm{T}} > 10$ GeV: the combination of the different algorithms ensures a $\sim 99\%$ efficiency to detect a muon over the full acceptance range. A candidate is also required to satisfy exactly the same isolation criteria (relative to its p_{T}) as for electrons.

C. Jets

Jets are reconstructed using the anti-k_t algorithm [88] with radius parameter $R = 0.4$ and are required to have $|\eta| < 4.4$ and satisfy (unless stated otherwise) $p_{\mathrm{T}} > 30$ GeV. Jets are discarded if they are within $\Delta R = 0.2$ of an isolated electron or within $\Delta R = 0.4$ of an isolated photon. The inputs to the jet-finding are topological calorimeter clusters [89] formed with the energy calibration appropriate for electromagnetic showers. The jet energy is calibrated using scale factors extracted from simulated dijet events by matching the energies of

the generator-level and reconstructed jets. In addition, for the 8 TeV data, the pileup dependence of the jet response is suppressed by subtracting the median E_{T} density for the event multiplied by the transverse area of the jet [90, 91]. A residual pileup correction that is proportional to the number of reconstructed primary vertices and to the average number of interactions per bunch crossing further reduces the pileup dependence, in particular in the forward region. Finally, the jet energy is corrected by an absolute scale factor determined using γ+jet, Z+jet and multijet events in data, and a relative η-dependent factor measured with dijet events in data. In order to suppress jets produced by pileup, jets within the tracking acceptance ($|\eta_j| < 2.4$) are required to have a jet vertex fraction[2] (JVF) [91] larger than 0.5 (0.25) for the 7 TeV (8 TeV) data, respectively.

In order to identify jets containing a b-hadron (b-jets), a NN-based algorithm is used to combine information from the tracks in a jet: the network exploits the measurements of the impact parameters of the tracks, any secondary vertices, and the outputs of decay topology algorithms as discussed in Refs. [92, 93]. Four different working points with efficiencies for identifying b-jets (rejection factors for light jets) of 60% (450), 70% (140), 80% (29), and 85% (11) are used in the analysis. The efficiencies and rejection factors at the working points are calibrated using control samples of data.

D. Missing transverse momentum

The measurement of the magnitude of the missing transverse momentum $E_{\mathrm{T}}^{\mathrm{miss}}$ is based on the transverse energy of all photon, electron and muon candidates, all jets sufficiently isolated from the photon, electron and muon candidates, and all calorimeter energy clusters not associated with any of these objects (*soft term*) [94]. In order to improve the discrimination of multijet events, where $E_{\mathrm{T}}^{\mathrm{miss}}$ arises mainly from energy resolution effects, from events with a large fraction of $E_{\mathrm{T}}^{\mathrm{miss}}$ due to non-interacting particles, an $E_{\mathrm{T}}^{\mathrm{miss}}$-significance is defined as $E_{\mathrm{T}}^{\mathrm{miss}}/\sigma_{E_{\mathrm{T}}^{\mathrm{miss}}}$, where the square root of the scalar sum of the transverse energies of all objects ΣE_{T} is used in the estimator of the $E_{\mathrm{T}}^{\mathrm{miss}}$ resolution $\sigma_{E_{\mathrm{T}}^{\mathrm{miss}}} = 0.67\,[\mathrm{GeV}^{1/2}]\sqrt{\Sigma E_{\mathrm{T}}}$. The proportionality factor $0.67\,[\mathrm{GeV}^{1/2}]$ is determined with fully reconstructed $Z \to \ell\ell$ events by removing the leptons in the measurement of $E_{\mathrm{T}}^{\mathrm{miss}}$ [95].

---

[2] The jet vertex fraction (JVF) is defined as the sum of p_{T} of the tracks associated with the jet that are produced at the diphoton's primary vertex, divided by the sum of p_{T} of the tracks associated with the jet from all collision vertices.

V. EVENT SELECTION

The measurement of the signal strengths of Higgs boson production is based on the extraction of resonance signals in the diphoton invariant mass spectra of 12 independent categories of events that are described in the next section. Common diphoton selection criteria are applied to all events. At least two photon candidates are required to be in a fiducial region of the EM calorimeter defined by $|\eta| < 2.37$, excluding the transition region between the barrel and the end-cap calorimeters ($1.37 < |\eta| < 1.56$). Photon candidates in this fiducial region are ordered according to their E_{T} and only the first two are considered: the leading and sub-leading photon candidates are required to have $E_{\mathrm{T}}/m_{\gamma\gamma} > 0.35$ and 0.25, respectively, where $m_{\gamma\gamma}$ is the invariant mass of the two selected photons. Requirements on the E_{T} of the two selected photons relative to $m_{\gamma\gamma}$ are found to give $m_{\gamma\gamma}$ spectra that are described by simpler parameterizations than for the constant cuts on E_{T} used in Ref. [13], as discussed in Sec. VII B.

The typical signal selection efficiency of the kinematic cuts described above ranges between 50% (for events from WH production) to 60% (for events from $t\bar{t}H$ production).

The invariant mass of the two photons is given by

$$m_{\gamma\gamma} = \sqrt{2E_1 E_2 (1 - \cos\,\alpha)},$$

where E_1 and E_2 are the energies of the leading and sub-leading photons and α is the opening angle of the two photons with respect to their production vertex. The selection of the correct diphoton production vertex is important for the resolution of the α measurement and thus for the precise measurement of $m_{\gamma\gamma}$. A position resolution on the diphoton production vertex of about 15 mm in the z direction with the photon trajectories measured by the EM calorimeter alone is achieved, which is sufficient to keep the contribution from the opening angle to the mass resolution smaller than the contribution from the energy resolution. However, an efficient procedure to select the diphoton production vertex among the primary vertex candidates reconstructed with the tracking detector is necessary. This selection allows the information associated with the primary vertex to be used to compute the track-based quantities used in the object definitions, such as the computation of photon isolation with tracks (Sec. IV A) and the selection of jets associated with the hard interaction (Sec. IV C).

The diphoton production vertex is selected from the reconstructed collision vertices using a neural-network algorithm. For each vertex the algorithm takes the following as input: the combined z-position of the intersections of the extrapolated photon trajectories (reconstructed by exploiting the longitudinal segmentation of the calorimeter) with the beam axis; the sum of the squared transverse momenta $\sum p_{\mathrm{T}}^2$ and the scalar sum of the transverse momenta $\sum p_{\mathrm{T}}$ of the tracks associated with the vertex;

the difference in azimuthal angle $\Delta\phi$ between the direction defined by the vector sum of the track momenta and that of the diphoton system. The trajectory of each photon is measured using the longitudinal segmentation of the calorimeter and a constraint from the average collision point of the proton beams. For converted photons, the position of the conversion vertex is also used if tracks from the conversion have hits in the silicon detectors.

The production vertex selection is studied with $Z \to ee$ events in data and simulation by removing the electron tracks from the events and then measuring the efficiency for finding the vertex associated with the Z boson production. The MC simulation is found to accurately describe the efficiency measured in data, as shown in Fig. 2. The efficiency for finding the reconstructed diphoton primary vertex ϵ_{PV} in simulated $H \to \gamma\gamma$ events from ggF production within 0.3 mm (15 mm) of the true vertex is around 85% (93%) over the typical range of the number of collision vertices per event observed in the 8 TeV data. The efficiency ϵ_{PV} increases for large diphoton p_T as the hadron system recoiling against the diphoton evolves into one or more jets, which in turn contain additional higher p_T tracks. These additional tracks make it more likely to reconstruct the diphoton vertex as a primary vertex. Therefore, by re-weighting the simulated $Z \to ee$ events to approximate the harder p_T spectrum of the simulated Higgs boson signal, ϵ_{PV} is well reproduced. The corresponding efficiencies for the 7 TeV data and MC samples are slightly higher, due to less pileup, and the efficiencies are as consistent as those for the 8 TeV data and MC samples.
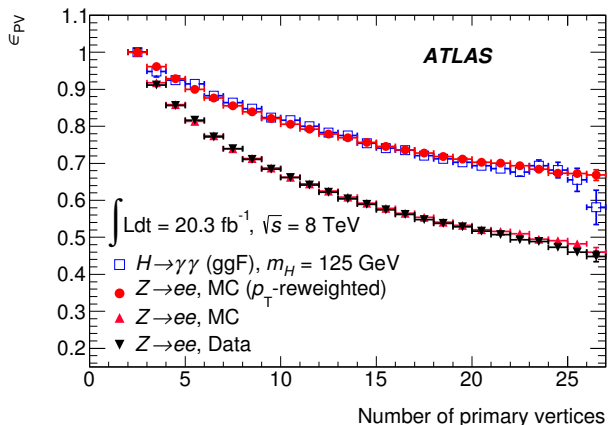

FIG. 2. Efficiency ϵ_{PV} to select a diphoton vertex within 0.3 mm of the production vertex as a function of the number of primary vertices in the event. The plot shows ϵ_{PV} for simulated ggF events (m_H=125 GeV) with two unconverted photons (hollow blue squares), for $Z \to ee$ events with the electron tracks removed for the neural network–based identification of the vertex, both in data (black triangles) and simulation (red triangles), and the same simulated $Z \to ee$ events re-weighted to reproduce the p_T spectrum of simulated ggF events (red circles).

A total of 94566 (17225) collision events at $\sqrt{s} = 8$ TeV (7 TeV) were selected with a diphoton invariant mass between 105 GeV and 160 GeV. The efficiency to select $H \to \gamma\gamma$ events is estimated using MC samples and found to range between 32% and 42%, depending on the production mode, as detailed in the following section.

VI. EVENT CATEGORIZATION

Gluon fusion is expected to be the dominant production mode of Higgs bosons at the LHC, contributing about 87% of the predicted total production cross section at $m_H = 125.4$ GeV and $\sqrt{s} = 7$–8 TeV, while VBF and the associated production processes VH and $t\bar{t}H$ are predicted to contribute only 7%, 5%, and 1%, respectively.

Based on their properties, the selected diphoton events (Sec. V) are divided into 12 categories, separately for each of the 7 TeV and 8 TeV datasets, that are optimized for sensitivity to the Higgs boson production modes studied here, for a Higgs boson mass of $m_H = 125$ GeV. The event selections are applied to the initial diphoton sample in sequence, as illustrated in Fig. 3. Only events that fail all the previous event selections are candidates for a given category, to ensure that the events are grouped into exclusive categories. The sequence of categories is chosen to give precedence to the production mechanisms that are expected to have the lowest signal yields. Each category is optimized by adjusting the event selection criteria to minimize the expected uncertainty in the signal strength of the targeted production process. Although the measurements are dominated by statistical uncertainties with the present dataset, systematic uncertainties are taken into account during the optimization.

The 12 exclusive categories, whose events have different signal invariant mass resolutions and signal-to-background ratios, can be logically grouped into four sets depending on the production processes they are expected to be most sensitive to, as described in the following subsections. Comparisons between signal MC samples, background MC samples, and data in the sidebands of the $m_{\gamma\gamma}$ distribution are shown for the main kinematic quantities used to define several of the categories. The sidebands throughout this analysis consist of the relevant candidate events with $m_{\gamma\gamma}$ in the ranges 105–120 GeV or 130–160 GeV.

A. Categories sensitive to $t\bar{t}H$

The two first categories are designed to select data samples enriched in leptonic and hadronic decays of top quark pairs, using the event selection described in Ref. [96]. Events in the $t\bar{t}H$ *leptonic* category are required to contain at least one electron or muon with $p_T > 15$ GeV or $p_T > 10$ GeV, respectively. Events are retained if either two or more b-jets are found or a single b-jet is found together with $E_T^{miss} \geq 20$ GeV. The b-jets

```
┌─────────────────────────┐
│   Diphoton selection    │
└─────────────────────────┘
             ↓
┌─────────────────────────┐
│      t̄tH leptonic       │
└─────────────────────────┘
             ↓
┌─────────────────────────┐
│      t̄tH hadronic       │
└─────────────────────────┘
             ↓
┌─────────────────────────┐
│      VH dilepton        │
│    (ZH → ℓℓH)           │
└─────────────────────────┘
             ↓
┌─────────────────────────┐
│      VH one-lepton      │
│    (WH → ℓνH)           │
└─────────────────────────┘
             ↓
┌─────────────────────────┐
│      VH E_T^miss        │
│  (ZH → ννH; WH → ℓνH)   │
└─────────────────────────┘
             ↓
┌─────────────────────────┐
│      VH hadronic        │
│  (WH → jjH; ZH → jjH)   │
└─────────────────────────┘
             ↓
┌─────────────────────────┐
│      VBF tight          │
│    (qqV → jjH)          │
└─────────────────────────┘
             ↓
┌─────────────────────────┐
│      VBF loose          │
│    (qqV → jjH)          │
└─────────────────────────┘
             ↓
┌─────────────────────────┐
│      Untagged           │
│    (gg → H)             │
└─────────────────────────┘
```
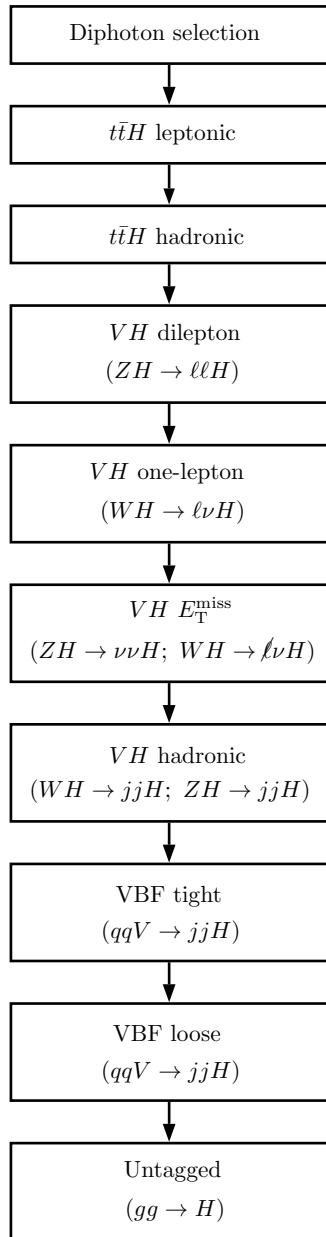
FIG. 3. Illustration of the order in which the criteria for the exclusive event categories are applied to the selected diphoton events. The division of the last category, which is dominated by ggF production, into four sub-categories is described in Sec. VI D.

are required to have $p_T \geq 25$ GeV and to be tagged using the 80% (85%) efficiency working point (WP) of the b-tagging algorithm [93] in the 8 TeV (7 TeV) data. In order to suppress the background contribution from Z+jets with $Z \to ee$, where a jet and an electron are misidentified as photons, events with an invariant electron–photon mass of 84–94 GeV are rejected.

Events in the $t\bar{t}H$ hadronic category are required not to have a well-reconstructed and identified lepton (electron or muon) passing the kinematic cuts described in

Sec. IV B. Also, they are required to fulfill at least one of the following sets of criteria that are partly based on the b-tagger, which is calibrated at several different working points of b-tagging efficiency (Sec. IV C):

1. at least six jets with $p_T > 25$ GeV out of which two are b-tagged using the 80% WP;

2. at least six jets with $p_T > 30$ GeV out of which one is b-tagged using the 60% WP;

3. at least five jets with $p_T > 30$ GeV out of which two are b-tagged using the 70% WP.

Only the first set of criteria above is applied to the 7 TeV data but with a working point efficiency of 85%.

The fraction of $t\bar{t}H$ events relative to all signal production passing this selection in the hadronic category is larger than 80% while in the leptonic category it ranges from 73% to 84% depending on the center-of-mass energy; the numbers are reported in Tables II and III. Contributions of about 10% from ggF events in the hadronic category and 10% from WH events in the leptonic category remain. The remaining 10% in each of the two categories is accounted for by tHW and $tHbj$ events.

B. Categories sensitive to VH

In the second step of the categorization the selection is optimized to identify events where a Higgs boson is produced in association with a Z or W boson. Compared with our previous studies, a new VH dilepton category is added to separately measure the signal strength parameters for the ZH and WH production modes in order to better test the custodial symmetry of the Higgs sector [13]. This new category exploits the dilepton decay of the Z boson by requiring two same-flavor opposite-sign leptons (electrons or muons) with $p_T > 15$ GeV and $p_T > 10$ GeV for electrons and muons, respectively. The invariant mass of the two leptons is required to be in the range 70–110 GeV. These requirements lead to a 99% signal-only purity for ZH production, the remaining 1% coming from $t\bar{t}H$ production (Tables II and III).

The VH one-lepton category is optimized to select events with a leptonic decay of the W boson by requiring the presence of one electron or muon with p_T greater than 15 GeV or 10 GeV, respectively. In order to exploit the missing transverse momentum signature of the neutrino in the decay chain, the significance of the missing transverse momentum, as defined in Sec. IV D, is required to be larger than 1.5. For the optimization of the selection cuts in this category, the expected background contribution is derived from data events in the sidebands. Approximately 90% of the signal events in this category are predicted to come from WH production, about 6% from ZH production, and 1–2% from $t\bar{t}H$ production.

The VH E_T^{miss} category is optimized to be enriched in events from VH production with a leptonic decay of a W boson, where the lepton is not detected or does not

pass the selection for the one-lepton category, or with a Z boson decay to two neutrinos. The minimal requirement on the significance of the missing transverse energy is 5.0, roughly equivalent to a direct requirement of $E_T^{miss} > 70$–100 GeV, depending on the value of $\sum E_T$. A further enrichment is obtained by requiring the magnitude p_{Tt} [97] of the component of the diphoton $\vec{p}_T$ transverse to its thrust axis in the transverse plane to be greater than 20 GeV. The p_{Tt} is used as a discriminant, rather than the p_T of the diphoton, because it is less affected by energy resolution and it is not correlated with the invariant mass of the diphoton. As for the VH one-lepton category, the background distributions for the cut optimizations are extracted from data events in the sidebands. After the event selection approximately 50% of the signal events in this category are predicted to come from ZH production, 40% from WH production, and the remaining 10% mainly from $t\bar{t}H$ production (Tables II and III).

The VH *hadronic* category consists of events that include the signature of a hadronically decaying vector boson. They are selected by requiring the presence of two reconstructed jets with a dijet invariant mass m_{jj} in the range 60–110 GeV. The sensitivity is further enhanced by requiring the difference between the pseudorapidities of the diphoton and the dijet systems $|\eta_{\gamma\gamma} - \eta_{jj}|$ to be less than one and the diphoton p_{Tt} greater than 70 GeV. The distributions of the discriminating variables used to define the VH hadronic category are shown in Fig. 4 for signal events from different production modes and for events from data and MC background. The MC background is composed of a mixture of $\gamma\gamma$, γ–jet and jet–jet samples normalized as discussed in Sec. VII B. Approximately 30% (20%) of the events in the VH hadronic category come from WH (ZH) production after the selection, while the remaining fraction is accounted for by ggF events surviving the selection cuts.

C. Categories sensitive to VBF

Signal events produced by the VBF mechanism are characterized by two well-separated jets with high transverse momentum and little hadronic activity between them. Events are preselected by requiring at least two reconstructed jets. The two leading jets $j1$ and $j2$ (those with the highest p_T) are required to satisfy $\Delta\eta_{jj} \geq 2.0$ and $|\eta^*| < 5.0$, where η^* is the pseudorapidity of the diphoton system relative to the average rapidity of the two leading jets $\eta^* \equiv \eta_{\gamma\gamma} - (\eta_{j1} + \eta_{j2})/2$ [98] and $\Delta\eta_{jj}$ is the pseudorapidity separation between the two leading jets. In order to optimize the sensitivity to VBF, a multivariate analysis exploits the full event topology by combining six discriminating variables into a single discriminant that takes into account the correlations among them. For this purpose a BDT is built with the following discriminating variables as input:

1. m_{jj}, the invariant mass of the two leading jets $j1$
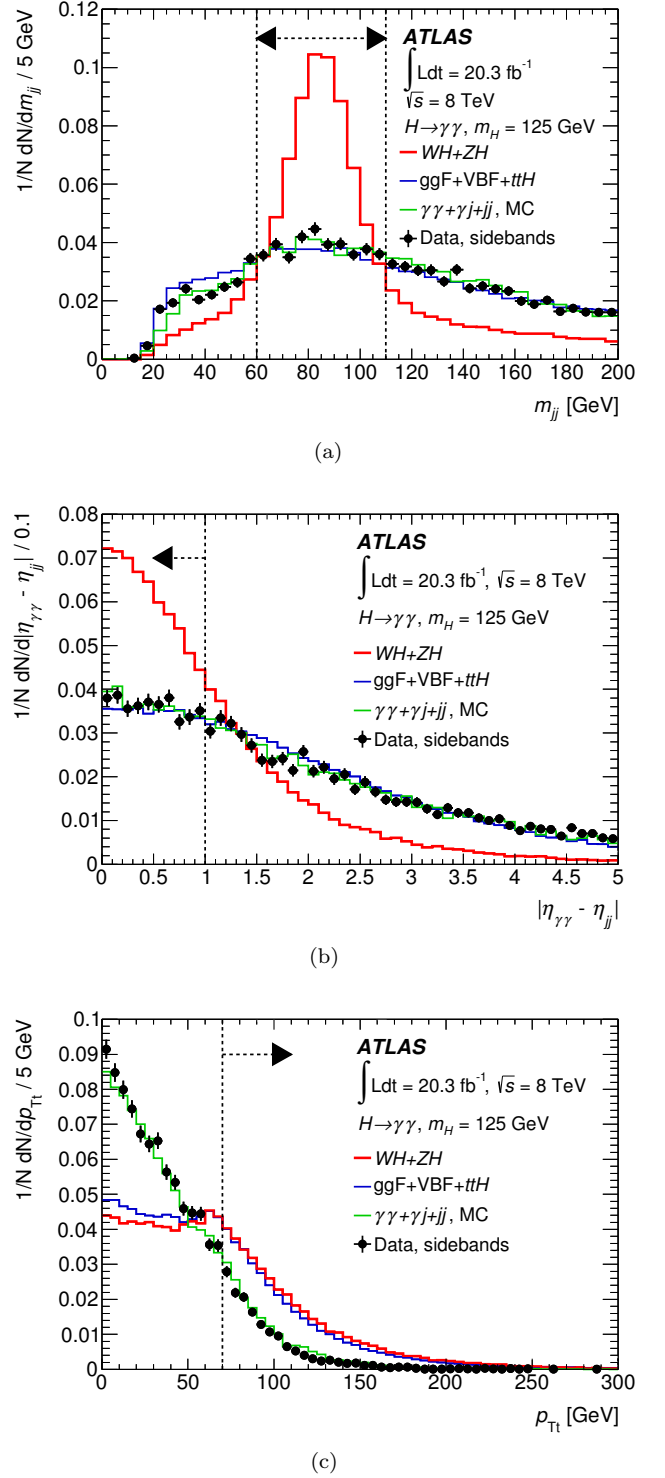
(a)

(b)

(c)

FIG. 4. Normalized distributions of the variables described in the text (Sec. VI B) used to sort diphoton events with at least two reconstructed jets into the VH hadronic category for the data in the sidebands (points), the predicted sum of the WH and ZH signals (red histograms), the predicted signal feed-through from ggF, VBF, and $t\bar{t}H$ production modes (blue histograms), and the simulation of the $\gamma\gamma$, γ–jet, and jet–jet background processes (green histograms). The arrows indicate the selection criteria applied to these observables. The mass of the Higgs boson in all signal samples is $m_H = 125$ GeV.

and j_2;

2. $\Delta\eta_{jj}$;

3. p_{Tt}, the p_{T} of the diphoton with respect to its thrust axis in the transverse plane;

4. $\Delta\phi_{\gamma\gamma,jj}$, the azimuthal angle between the diphoton and the dijet systems;

5. $\Delta R_{\gamma,j}^{\mathrm{min}}$, the minimum separation between the leading/subleading photon and the leading/subleading jet;

6. η^*.

After the preselection, these variables are found to have little or no correlation to $m_{\gamma\gamma}$, thus ensuring that no biases in the final diphoton mass fit are introduced. The individual separation power between VBF and ggF and prompt $\gamma\gamma$, γ–jet and jet–jet events is illustrated in Fig. 5 for each discriminating variable.

The signal sample used to train the BDT is composed of simulated VBF events, while a mixture of samples is used for the background: a sample of simulated ggF events, a sample of prompt diphoton events generated with SHERPA for the irreducible background component, and events from data in which one or both photon candidates fail to satisfy the isolation criteria for the reducible γ–jet and jet–jet components. The contribution from ggF to the background sample is normalized to the rate predicted by the SM. The other background components are weighted in order to reproduce the background composition measured in the data (see Sec. VII B).

Events are sorted into two categories with different VBF purities according to the output value of the BDT, O_{BDT}:

1. VBF tight: $O_{\mathrm{BDT}} \geq 0.83$;

2. VBF loose: $0.3 < O_{\mathrm{BDT}} < 0.83$.

Figure 6 shows the distributions of O_{BDT} for the VBF signal, feed-through from ggF production, the simulated continuum background, and data from the sidebands. The O_{BDT} distributions of the background MC prediction and the data in the sidebands are in good agreement. As an additional cross-check, the BDT is applied to a large sample of $Z(\to ee)$+jets in data and MC samples. The resulting O_{BDT} distributions are found to be in excellent agreement. The fraction of VBF events in the VBF tight (loose) category is approximately 80% (60%), the remaining 20% (40%) being contributed by ggF events. An increase of about 6% in the fraction of VBF events assigned to the VBF categories is obtained with the present optimization with respect to our previously published results [13].

D. Untagged categories

Compared with our previously published analysis, the categorization of the events that are not assigned to the $t\bar{t}H$, VH or VBF categories is simplified by reducing the number of *untagged* categories from nine to four with no increase in the signal strength uncertainty. The category definition is based on the p_{Tt} of the diphoton system and the pseudorapidities of the photons:

1. *Central - low p_{Tt}*: $p_{\mathrm{Tt}} \leq 70$ GeV and both photons have $|\eta| < 0.95$;

2. *Central - high p_{Tt}*: $p_{\mathrm{Tt}} > 70$ GeV and both photons have $|\eta| < 0.95$;

3. *Forward - low p_{Tt}*: $p_{\mathrm{Tt}} \leq 70$ GeV and at least one photon has $|\eta| \geq 0.95$;

4. *Forward - high p_{Tt}*: $p_{\mathrm{Tt}} > 70$ GeV and at least one photon has $|\eta| \geq 0.95$.

This categorization of the untagged events increases the signal-to-background ratio of the events with high p_{Tt} with a gain of about a factor of three (two) for central (forward) categories with respect to low p_{Tt} events, as illustrated in Fig. 7. Since the MC background is not used directly in the analysis, the slight mis-modeling observed in the high-p_{Tt} region does not bias the signal measurement, causing only a suboptimal choice of the discriminating cut. The typical fraction of ggF events in the low (high) p_{Tt} categories is 90% (70%). The remaining 10% (30%) is equally accounted for by the contribution from VBF events and the sum of all the remaining processes.

E. Summary of categories

The predicted signal efficiencies, which include geometrical and kinematic acceptances, and event fractions per production mode in each event category for $m_H = 125.4$ GeV are listed in Tables II and III for the 7 TeV and 8 TeV data, respectively. The total expected numbers of signal events per event category N_{S} are also shown, normalized as discussed in Sec. III.

The dependence of the yield for each production process on the Higgs boson mass is parameterized in each category with simple polynomials that are used to build the statistical model described in Sec. IX. As discussed in Sec. III, the detection efficiency for $b\bar{b}H$ events is assumed to be the same as for ggF events. The expected contamination of ggF and VBF in the VH $E_{\mathrm{T}}^{\mathrm{miss}}$ category is larger in 7 TeV data than in 8 TeV data due to the poorer resolution of the $E_{\mathrm{T}}^{\mathrm{miss}}$ reconstruction algorithm used in the 7 TeV analysis.

The number of events observed in data in each category is reported in Table IV separately for the 7 TeV and 8 TeV data. The impact of the event categorization described in the previous sections on the uncertainty in the combined signal strength is estimated on a representative
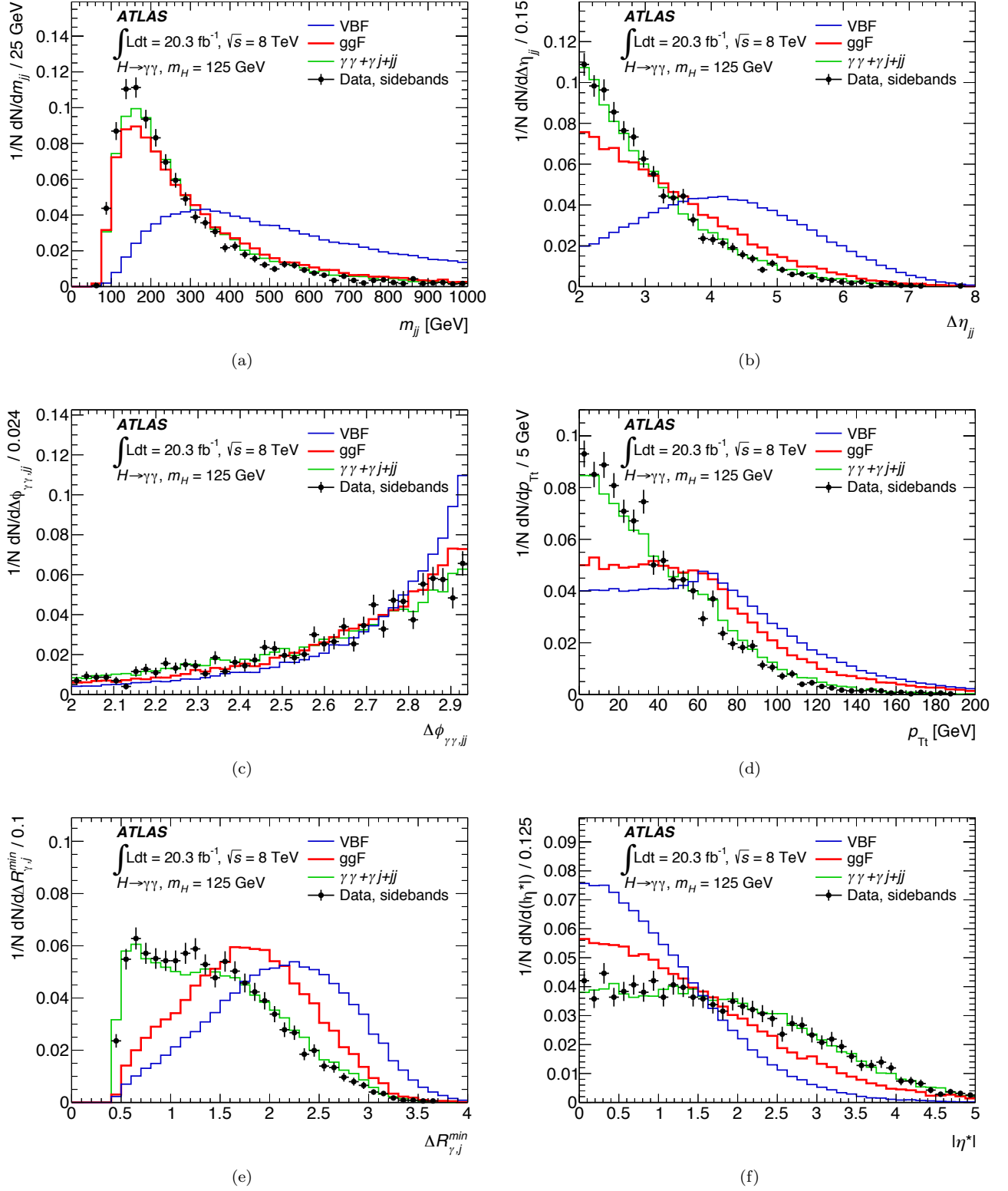
FIG. 5. Normalized kinematic distributions of the six variables describe in the text (Sec. VI C) used to build the BDT that assigns events to the VBF categories, for diphoton candidates with two well-separated jets ($\Delta\eta_{jj} \geq 2.0$ and $|\eta^*| < 5.0$). Distributions are shown for data sidebands (points) and simulation of the VBF signal (blue histograms), feed-through from ggF production (red histograms), and the continuum QCD background predicted by MC simulation and data control regions (green histograms) as described in the text. The signal VBF and ggF samples are generated with a Higgs boson mass $m_H = 125$ GeV.

TABLE II. Signal efficiencies ϵ, which include geometrical and kinematic acceptances, and expected signal event fractions f per production mode in each event category for $\sqrt{s} = 7$ TeV and $m_H = 125.4$ GeV. The second-to-last row shows the total efficiency per production process summed over the categories and the overall average efficiency in the far right column. The total number of selected signal events expected in each category N_S is reported in the last column while the total number of selected events expected from each production mode is given in the last row.

| | ggF | | VBF | | WH | | ZH | | $t\bar{t}H$ | | bbH | | $tHbj$ | | tHW | | |
Category	$\epsilon(\%)$	$f(\%)$	$\epsilon(\%)$	$f(\%)$	$\epsilon(\%)$	$f(\%)$	$\epsilon(\%)$	$f(\%)$	$\epsilon(\%)$	$f(\%)$	$\epsilon(\%)$	$f(\%)$	$\epsilon(\%)$	$f(\%)$	$\epsilon(\%)$	$f(\%)$	N_S
Central - low p_{Tt}	15.5	92.2	8.5	4.1	7.2	1.6	7.9	1.0	3.4	0.1	15.5	1.0	-	-	-	-	26.0
Central - high p_{Tt}	1.0	71.8	2.7	16.4	2.1	6.1	2.3	3.7	2.9	1.2	1.0	0.7	-	-	-	-	2.1
Forward - low p_{Tt}	23.3	91.5	13.2	4.2	13.5	2.0	14.3	1.2	4.3	0.1	23.3	0.9	-	-	-	-	39.5
Forward - high p_{Tt}	1.3	70.6	4.0	16.7	3.5	6.9	3.6	4.1	2.9	0.9	1.3	0.7	-	-	-	-	3.0
VBF loose	0.4	38.6	7.9	60.0	0.2	0.6	0.2	0.3	0.2	0.1	0.4	0.4	-	-	-	-	1.7
VBF tight	0.1	18.1	6.3	81.5	<0.1	0.1	<0.1	0.1	0.1	<0.1	0.1	0.2	-	-	-	-	1.0
VH hadronic	0.2	43.5	0.1	3.3	3.2	31.8	3.4	19.8	0.9	1.3	0.2	0.4	-	-	-	-	0.6
VH E_T^{miss}	<0.1	8.7	0.1	3.7	1.7	35.7	3.6	44.8	2.3	7.1	<0.1	0.1	-	-	-	-	0.3
VH one-lepton	<0.1	0.7	<0.1	0.2	5.0	91.4	0.6	5.9	0.7	1.8	<0.1	<0.1	-	-	-	-	0.3
VH dilepton	<0.1	<0.1	<0.1	<0.1	<0.1	<0.1	1.3	99.3	<0.1	0.6	<0.1	<0.1	-	-	-	-	0.1
$t\bar{t}H$ hadronic	<0.1	10.5	<0.1	1.3	<0.1	1.3	<0.1	1.4	6.1	81.0	<0.1	0.1	1.5	2.6	4.3	1.9	0.1
$t\bar{t}H$ leptonic	<0.1	0.6	<0.1	0.1	0.3	14.9	0.1	4.0	8.5	72.6	<0.1	<0.1	4.8	5.3	8.7	2.5	0.1
Total efficiency (%)	41.8	-	42.9	-	36.7	-	37.3	-	32.2	-	41.8	-	-	-	-	-	41.6%
Events	64.8		5.4		2.2		1.3		0.3		0.7		<0.1		<0.1		74.5

TABLE III. Signal efficiencies ϵ, which include geometrical and kinematic acceptances, and expected signal event fractions f per production mode in each event category for $\sqrt{s} = 8$ TeV and $m_H = 125.4$ GeV. The second-to-last row shows the total efficiency per production process summed over the categories and the overall average efficiency in the far right column. The total number of selected signal events expected in each category N_S is reported in the last column while the total number of selected events from each production mode is given in the last row.

| | ggF | | VBF | | WH | | ZH | | $t\bar{t}H$ | | bbH | | $tHbj$ | | tHW | | |
Category	$\epsilon(\%)$	$f(\%)$	$\epsilon(\%)$	$f(\%)$	$\epsilon(\%)$	$f(\%)$	$\epsilon(\%)$	$f(\%)$	$\epsilon(\%)$	$f(\%)$	$\epsilon(\%)$	$f(\%)$	$\epsilon(\%)$	$f(\%)$	$\epsilon(\%)$	$f(\%)$	N_S
Central - low p_{Tt}	14.1	92.3	7.5	4.0	6.5	1.5	7.2	1.0	2.9	0.1	14.1	1.0	-	-	-	-	135.5
Central - high p_{Tt}	0.9	73.3	2.5	15.7	1.9	5.5	2.0	3.4	2.4	1.3	0.9	0.8	-	-	-	-	11.3
Forward - low p_{Tt}	21.6	91.7	11.9	4.1	12.3	1.9	13.0	1.2	3.8	0.1	21.6	1.0	-	-	-	-	208.6
Forward - high p_{Tt}	1.3	71.9	3.6	16.2	3.2	6.4	3.3	3.9	2.5	0.9	1.3	0.8	-	-	-	-	16.1
VBF loose	0.4	41.9	7.2	56.5	0.2	0.6	0.2	0.4	0.2	0.1	0.4	0.4	-	-	-	-	9.3
VBF tight	0.1	19.0	6.4	80.5	<0.1	0.2	<0.1	0.1	0.1	0.1	0.1	0.2	-	-	-	-	5.7
VH hadronic	0.2	45.9	0.1	3.2	3.0	30.3	3.1	18.8	0.7	1.3	0.2	0.5	-	-	-	-	3.2
VH E_T^{miss}	<0.1	2.3	<0.1	0.3	1.3	36.9	3.0	51.0	1.8	9.5	<0.1	<0.1	-	-	-	-	1.1
VH one-lepton	<0.1	0.5	<0.1	0.2	4.8	89.8	0.6	6.3	1.0	3.3	<0.1	<0.1	-	-	-	-	1.7
VH dilepton	<0.1	<0.1	<0.1	<0.1	<0.1	<0.1	1.3	99.1	<0.1	0.9	<0.1	<0.1	-	-	-	-	0.3
$t\bar{t}H$ hadronic	<0.1	7.3	<0.1	1.0	<0.1	0.7	<0.1	1.3	6.9	84.1	<0.1	<0.1	2.1	3.4	4.8	2.1	0.5
$t\bar{t}H$ leptonic	<0.1	1.0	<0.1	0.2	0.1	8.1	0.1	2.3	7.9	80.3	<0.1	<0.1	4.1	5.5	7.1	2.6	0.6
Total efficiency (%)	38.7	-	39.1	-	33.3	-	33.8	-	30.2	-	38.7	-					38.5%
Events	342.8		28.4		10.7		6.4		1.8		3.6		<0.1		<0.1		393.8
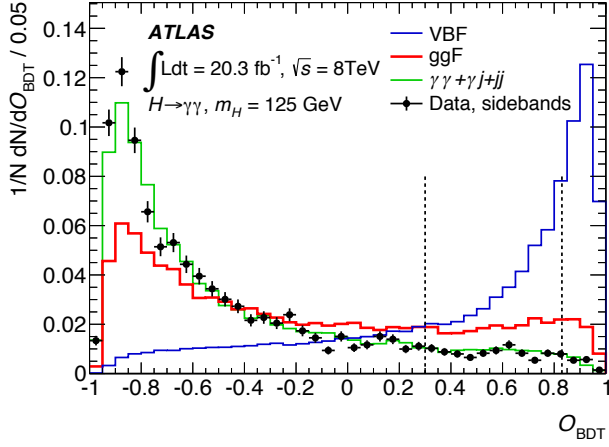
FIG. 6. Probability distributions of the output of the BDT O_{BDT} for the VBF signal (blue), ggF feed-through (red), continuum QCD background predicted by MC samples and data control regions (green) as described in the text, and data sidebands (points). The two vertical dashed lines indicate the cuts on O_{BDT} that define the VBF loose and VBF tight categories. The signal VBF and ggF samples are generated with a Higgs boson mass $m_H = 125$ GeV.

signal plus MC background sample generated under the SM hypothesis ($\mu = 1$): the event categorization is found to provide a 20% reduction of the total uncertainty with respect to an inclusive analysis.

TABLE IV. Number of selected events in each event category for the 7 TeV and 8 TeV data and with a diphoton candidate invariant mass between 105 GeV and 160 GeV.

Category	$\sqrt{s} = 7$ TeV	$\sqrt{s} = 8$ TeV
Central - low p_{Tt}	4400	24080
Central - high p_{Tt}	141	806
Forward - low p_{Tt}	12131	66394
Forward - high p_{Tt}	429	2528
VBF loose	58	411
VBF tight	7	67
VH hadronic	34	185
VH $E_{\mathrm{T}}^{\mathrm{miss}}$	14	35
VH one-lepton	5	38
VH dilepton	0	2
$t\bar{t}H$ hadronic	3	15
$t\bar{t}H$ leptonic	3	5

VII. SIGNAL AND BACKGROUND MODELS

The $m_{\gamma\gamma}$ distribution of the data in each category is fitted with the sum of a signal model plus an analytic parameterization of the background. The signal and background models are described in this section.
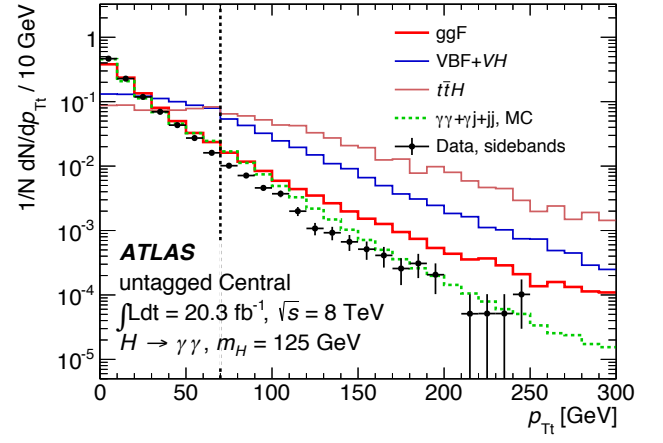
(a)
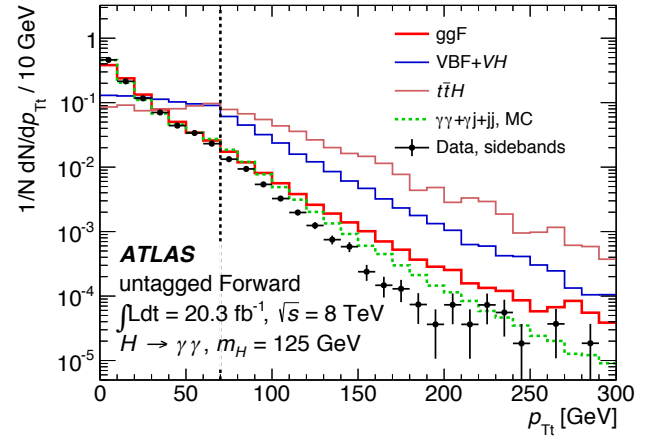
(b)

FIG. 7. Distributions of the component of the diphoton $\vec{p}_{\mathrm{T}}$ transverse to its thrust axis in the transverse plane p_{Tt} for diphoton candidates in the sidebands in the untagged (a) Central and (b) Forward categories for $\sqrt{s} = 8$ TeV for predicted Higgs boson production processes (solid histograms), the predicted sum of prompt $\gamma\gamma$, γ–jet and jet–jet background processes (green histogram), and data (points). The vertical dashed lines indicate the value used to classify events into the low- or high-p_{Tt} categories. The mass for all Higgs boson signal samples is $m_H = 125$ GeV.

A. Signal model

The normalized distribution of $m_{\gamma\gamma}$ for signal events in each category c is described by a composite model $f_{\mathrm{S},c}$ resulting from the sum of a Crystal Ball function $f_{\mathrm{CB},c}$ [99] (a Gaussian core with one exponential tail) and a small, wider Gaussian component $f_{\mathrm{GA},c}$. The function $f_{\mathrm{CB},c}$ represents the core of well-reconstructed events, while the Gaussian component $f_{\mathrm{GA},c}$ is used to describe the outliers of the distribution. The signal model for a given

event category and value of m_H can be written as:

$$f_{\text{S},c}(m_{\gamma\gamma}, \mu_{\text{CB},c}, \sigma_{\text{CB},c}, \alpha_{\text{CB},c}, n_{\text{CB}}, \phi_{\text{CB},c}, \mu_{\text{GA},c}, \sigma_{\text{GA},c})$$
$$= \phi_{\text{CB},c}\, f_{\text{CB},c}(m_{\gamma\gamma}, \mu_{\text{CB},c}, \sigma_{\text{CB},c}, \alpha_{\text{CB},c}, n_{\text{CB}})$$
$$+ (1 - \phi_{\text{CB},c})f_{\text{GA},c}(m_{\gamma\gamma}, \mu_{\text{GA},c}, \sigma_{\text{GA},c}), \quad (1)$$

where $\mu_{\text{CB},c}$, $\sigma_{\text{CB},c}$ are the peak position and the width of the Gaussian core of the Crystal Ball function

$$f_{\text{CB},c}(m_{\gamma\gamma}, \mu_{\text{CB},c}, \sigma_{\text{CB},c}, \alpha_{\text{CB},c}, n_{\text{CB}}) = \mathcal{N}_c \begin{cases} e^{-t^2/2} & t > -\alpha_{\text{CB},c}, \\ \left(\frac{n_{\text{CB}}}{|\alpha_{\text{CB},c}|}\right)^{n_{\text{CB}}} e^{-|\alpha_{\text{CB},c}|^2/2} \left(\frac{n_{\text{CB}}}{\alpha_{\text{CB},c}} - \alpha_{\text{CB},c} - t\right)^{-n_{\text{CB}}} & t < -\alpha_{\text{CB},c}, \end{cases}$$

where $t = (m_{\gamma\gamma} - \mu_{\text{CB},c})/\sigma_{\text{CB},c}$, $\mathcal{N}_c$ normalizes the distribution, and $\mu_{\text{GA},c}$, $\sigma_{\text{GA},c}$ are the peak position and the width of the Gaussian component of the model due to the outliers ($\mu_{\text{CB},c}$ and $\mu_{\text{GA},c}$ are fitted independently but both take on values close to m_H). The non-Gaussian tail of $f_{\text{CB},c}$ is parameterized by $\alpha_{\text{CB},c}$ and n_{CB}. The fraction of the composite model due to the Crystal Ball component is described by $\phi_{\text{CB},c}$.

Since the model parameters exhibit a smooth dependence on the values of m_H in the simulated signal samples, the precision of the fit results is improved by assuming a polynomial dependence of the parameters on m_H. The coefficients of the polynomials, except for n_{CB}, which is fixed to a constant value for all categories, are determined for each event category by a simultaneous fit to the relevant sets of simulated signal mass peaks (Sec. III) weighted by their contributions to the signal yield expected in the SM. For example, $\mu_{\text{CB},c}$ is to a good approximation found to be equal to the test value of m_H. The model parameters extracted for $m_H = 125.4$ GeV are inputs to the extended likelihood function described in Sec. IX.

The invariant mass resolutions σ_{68}, defined as half of the smallest $m_{\gamma\gamma}$-interval containing 68% of the signal events, for the 12 event categories are in the range 1.32–1.86 GeV (1.21–1.69 GeV) for the 8 TeV (7 TeV) data at $m_H = 125.4$ GeV. They are reported in Table V. The slightly smaller invariant mass resolution in the 7 TeV signal samples arises from a different effective constant term in the energy resolution measured with $Z \rightarrow ee$ events and from the lower pileup level in the 7 TeV data [15].

The $m_{\gamma\gamma}$ distributions of simulated signal events generated with $m_H = 125$ GeV at $\sqrt{s} = 8$ TeV assigned to the categories with the best (Central - high p_{Tt}) and worst mass resolution (Forward - low p_{Tt}) are shown in Fig. 8 together with the signal models resulting from the simultaneous fits described above. The signal resolution predicted by the MC simulation varies by less than 10% over the full range of pileup conditions in the analyzed data, as shown in Fig. 9. This figure also shows the predicted signal resolution obtained using the two primary vertex algorithms discussed in Sec. V compared with the

TABLE V. Effective signal mass resolutions σ_{68} and σ_{90} for the 7 TeV and 8 TeV data in each event category, where σ_{68} (σ_{90}) is defined as half of the smallest interval expected to contain 68% (90%) of the signal events (N_{S} in Table III) for a mass $m_H = 125.4$ GeV.

Category	$\sqrt{s}$=7 TeV		$\sqrt{s}$=8 TeV	
	σ_{68} [GeV]	σ_{90} [GeV]	σ_{68} [GeV]	σ_{90} [GeV]
Central - low p_{Tt}	1.36	2.32	1.47	2.50
Central - high p_{Tt}	1.21	2.04	1.32	2.21
Forward - low p_{Tt}	1.69	3.03	1.86	3.31
Forward - high p_{Tt}	1.48	2.59	1.64	2.88
VBF loose	1.43	2.53	1.57	2.78
VBF tight	1.37	2.39	1.47	2.61
VH hadronic	1.35	2.32	1.45	2.57
VH $E_{\text{T}}^{\text{miss}}$	1.41	2.44	1.56	2.74
VH one-lepton	1.48	2.55	1.61	2.80
VH dilepton	1.45	2.59	1.59	2.76
$t\bar{t}H$ hadronic	1.39	2.37	1.53	2.64
$t\bar{t}H$ leptonic	1.42	2.45	1.56	2.69

ideal case in which the true vertex from the MC simulation is used.

B. Background models

The background parameterizations are selected using MC samples or control samples of data as described in the following.

For the four untagged, the two VBF, the VH hadronic and $E_{\text{T}}^{\text{miss}}$ categories, the background parameterizations are tested with a mixture of $\gamma\gamma$, γ–jet and jet–jet samples with the detector response simulated using the simplified models mentioned in Sec. III. The numbers of $\gamma\gamma$, γ–jet and jet–jet events in the selected diphoton event sample are estimated by means of a double two-dimensional sideband method. The event fractions are fitted to the distribution of the numbers of events in two bins of loose and tight photon identification criteria times two bins of loose and tight photon isolation criteria, for each of the two photon candidates per event. The method relies on the negligible correlation between
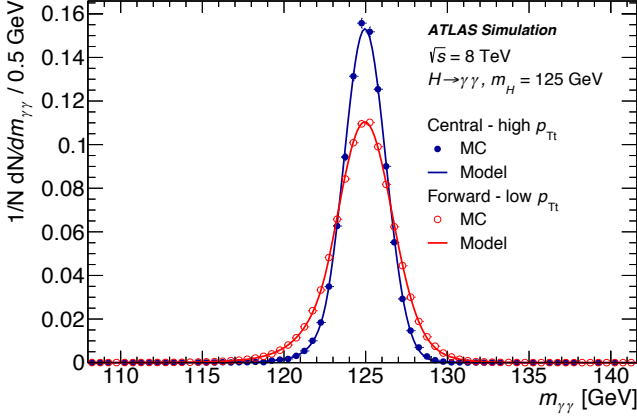
FIG. 8. Distributions of diphoton invariant mass $m_{\gamma\gamma}$ in a sample of Higgs boson events generated with $m_H = 125$ GeV at $\sqrt{s} = 8$ TeV in the categories with the best resolution (Central - high p_{Tt}, $\sigma_{68} = 1.32$ GeV) and worst resolution (Forward - low p_{Tt}, $\sigma_{68} = 1.86$ GeV) together with the signal models resulting from the simultaneous fits described in the text.
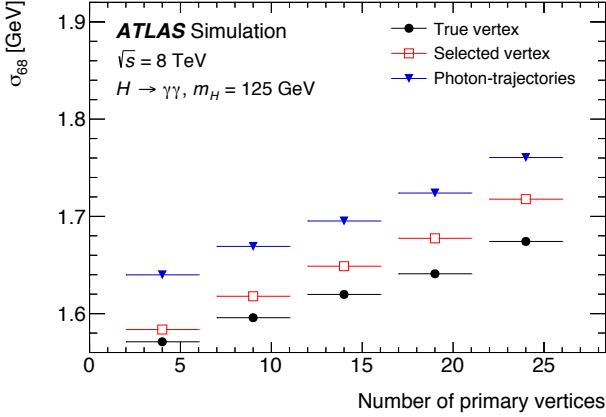

FIG. 9. Signal invariant mass resolution σ_{68} (defined in the text) as a function of the number of primary vertices per event when using the true diphoton production vertex from the MC simulation (points), the production vertex reconstructed by the multivariate algorithm described in Sec. V (open squares), and the production vertex reconstructed using only the photon trajectories (triangles). The events from different production processes are weighted according the SM cross sections and are required to fulfill the diphoton selection criteria (Sec. V) with no categorization applied.

these two variables for the jet background and that the sidebands (the regions where either the photon identification or isolation is loose) are essentially populated by jets. The small signal contamination in the control regions is estimated using the MC simulation and accounted for. The method is cross-checked with alternative in situ techniques as described in Refs. [100, 101]. The number of events for each component in the selected

diphoton events sample, obtained independently in each bin of $m_{\gamma\gamma}$, is shown in Fig. 10. The fractions of the
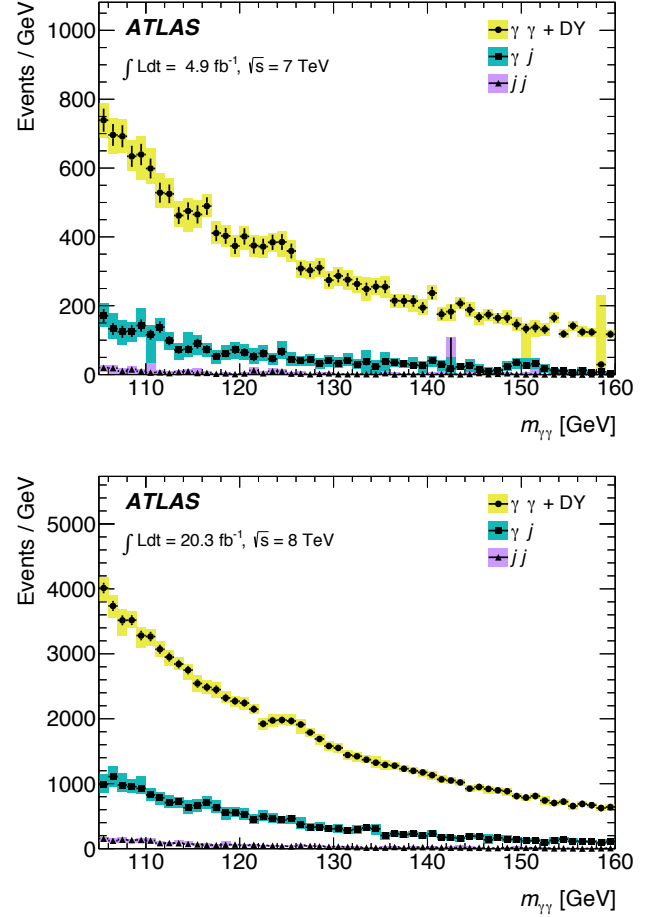
FIG. 10. Cumulative components (jet–jet, γ–jet and $\gamma\gamma$) of the inclusive diphoton invariant mass spectrum, estimated using the double two-dimensional sideband method as described in the text, in 7 TeV and 8 TeV data for all events passing the diphoton event selection. The $\gamma\gamma$ component also includes a small e^+e^- contribution from the Drell–Yan process. The error bars on each point represent the statistical uncertainty on the measurement while the colored bands represent the total uncertainty.

three contributions, integrated over the $m_{\gamma\gamma}$ spectrum, are found to be 84±8% (77±3%), 15±8% (20±2%), and 1±1% (3±1%) for the 7 TeV (8 TeV) data, respectively. The MC components mentioned above are combined according to these fractions and different background templates are derived for each category by applying the specific event selection of the category. The combined background samples are then normalized to the numbers of events observed in these categories (Table IV). Since this representative background sample for each category contains many times more events than the corresponding data sample, the invariant mass distribution normalized to the data has negligible statistical fluctuations relative to the statistical uncertainties that are taken from the

data. Median expectations for quantities such as signal significance, signal amplitude, and their uncertainties are estimated using a single fit to the representative background sample [102]. Other components that contribute less than 1% of the total background, such as Drell–Yan and $W\gamma$ and $Z\gamma$ production, are neglected. For the VH $E_{\rm T}^{\rm miss}$ category, since the effect of the $E_{\rm T}^{\rm miss}$ cut on the background shape is found to be negligible, it is not applied to the MC events. The background samples for the VH one-lepton category are obtained from the MC $\gamma\gamma$ and γ–jet events introduced previously, where one jet is treated as a lepton for the category selection.

An example of the diphoton invariant mass distributions in data and a MC background sample is shown in Fig. 11 for the Central - low $p_{\rm Tt}$ category. For each category, the simulation describes the distributions of the data sufficiently well (apart from the signal region $m_{\gamma\gamma} \sim 125$ GeV) to be used to select the parameterization of the background model and to assess the corresponding systematic uncertainty on the signal yield.
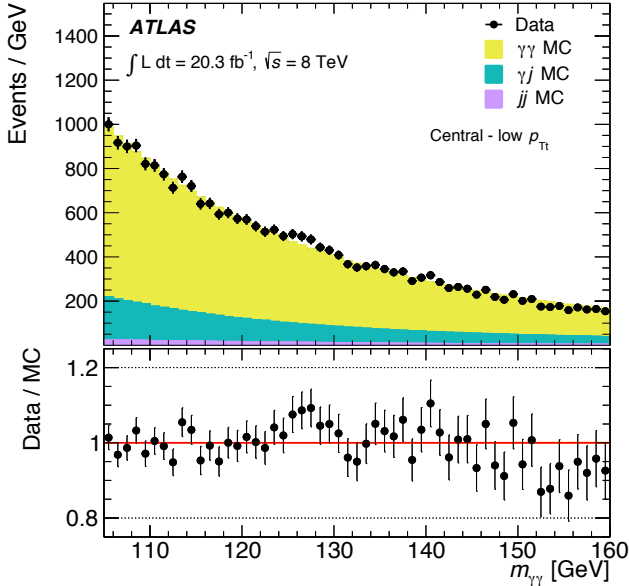
FIG. 11. The distributions of diphoton invariant mass $m_{\gamma\gamma}$ in the untagged Central - low $p_{\rm Tt}$ category in data (points), and MC samples for the jet–jet, γ–jet and $\gamma\gamma$ components of the continuum background (shaded cumulative histograms). The lower plot shows the ratio of data to MC simulation.

A sample of fully simulated $Z\gamma\gamma$ events is used for the VH dilepton category since the contributions from $Z\gamma$+jets and Z+jets events are estimated to be negligible after the event selection. For the $t\bar{t}H$ categories, the background parameterizations are tested on data control samples obtained by inverting photon identification criteria, isolation and the b-tagging, replacing the electron(s) with jet(s) and/or loosening the requirement on the number of jets.

The selection of the parameterization for the back-ground model proceeds as follows. The distributions of $m_{\gamma\gamma}$ from the samples described above are fitted in the same 105–160 GeV range as the data with a signal at a given m_H (as described in Sec. VII A) plus a background model. Since no signal is present in those background-only samples, the resulting number of signal events from the fit $N_{\rm sp}(m_H)$ is taken as an estimate of the bias in a particular background model under test. For such a bias to be considered acceptable, $N_{\rm sp}(m_H)$ has to be much smaller than the expected signal rate or much smaller than the statistical uncertainty on the number of background events in the fitted signal peak $\sigma_{\rm bkgd}(m_H)$, for cases where the number of expected signal events is very small. The following criteria are adopted:

$$|N_{\rm sp}(m_H)| < 10\% \, N_{\rm S,exp}(m_H)$$
$$\text{or}$$
$$|N_{\rm sp}(m_H)| < 20\% \, \sigma_{\rm bkgd}(m_H) \tag{2}$$

for all m_H in the mass range 119–135 GeV. The mass range was decided a priori to cover a region of approximately five times the expected signal mass resolution on either side of the value of m_H measured by ATLAS in the $H \to \gamma\gamma$ channel [13]. Here $N_{\rm S,exp}(m_H)$ is the number of signal events for a given value of m_H expected to pass the $H \to \gamma\gamma$ selection. For a given category, the parameterization with the smallest number of free parameters satisfying the criteria in Eq. (2) is chosen as background model.

As an illustration of the procedure, the ratio $\mu_{\rm sp}(m_H)$ of $N_{\rm sp}(m_H)$ to the expected number of signal events is shown in Fig. 12 for different candidate background models as functions of the test mass m_H for the Central - low $p_{\rm Tt}$ category. The candidate parameterizations include exponentials of first-, second- or third-order polynomials (exp1, exp2, exp3) and third-, fourth- or fifth-order Bernstein polynomials [103] (bern3, bern4, bern5). The bands representing the criteria in Eq. (2) are also shown. In this category exp1 and bern3 are excluded by the selection procedure and exp2 is chosen since it has the fewest degrees of freedom of the parameterizations that satsify the selection criteria.

The largest $N_{\rm sp}(m_H)$ in the mass range 119–135 GeV of a chosen parameterization, the *spurious signal* $N_{\rm spur}$, is assigned as the systematic uncertainty on the signal amplitude due to the background modeling. Table VI summarizes the parameterizations used for the background model in each category described in Sec. VI together with the derived uncertainties in terms of both spurious signal and its ratio to the predicted number of signal events in each category ($\mu_{\rm spur}$).

The numbers of measured background events B_{90} within windows of invariant mass expected to contain 90% of the numbers of signal events predicted by the SM S_{90} are listed in Table VII together with the expected signal purity $S_{90}/(S_{90} + B_{90})$ and signficance $S_{90}/\sqrt{S_{90} + B_{90}}$, for each event category and the 7 TeV and 8 TeV datasets.
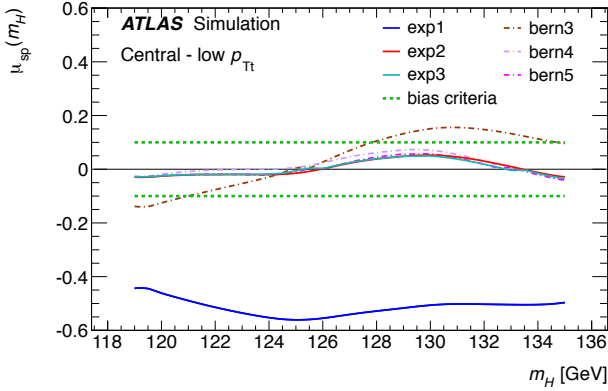
FIG. 12. Ratio of the fitted number of signal events to the number expected for the SM $\mu_{\rm sp}(m_H)$ as a function of the test mass m_H for the untagged Central - low $p_{\rm Tt}$ category. A single fit per value of m_H is performed on the represenative pure MC background sample described in the text with signal plus a variety of background parameterizations (exp1, exp2, exp3 for the exponentials of first, second or third-order polynomials, respectively, and bern3, bern4, bern5 for third, fourth and fifth-order Bernstein polynomials, respectively). The bias criteria in Eq. (2) are indicated by the dashed lines.

TABLE VI. List of the functions chosen to model the background distributions of $m_{\gamma\gamma}$ and the associated systematic uncertainties on the signal amplitudes in terms of spurious signal ($N_{\rm spur}$) and its ratio to the predicted number of signal events in each category ($\mu_{\rm spur}$) for the 12 categories and the 7 TeV and 8 TeV datasets. Model exp1 (exp2) is the exponential of a first-order (second-order) polynomial.

| Category | Model | $\sqrt{s} = 7$ TeV | | $\sqrt{s} = 8$ TeV | |
		$N_{\rm spur}$	$\mu_{\rm spur}$	$N_{\rm spur}$	$\mu_{\rm spur}$
Central - low $p_{\rm Tt}$	exp2	1.1	0.041	6.7	0.050
Central - high $p_{\rm Tt}$	exp1	0.1	0.029	0.4	0.036
Forward - low $p_{\rm Tt}$	exp2	0.6	0.016	7.0	0.034
Forward - high $p_{\rm Tt}$	exp2	0.3	0.088	1.2	0.073
VBF loose	exp1	0.2	0.091	1.3	0.14
VBF tight	exp1	< 0.1	0.031	0.3	0.054
VH hadronic	exp1	0.1	0.14	0.5	0.14
VH $E_{\rm T}^{\rm miss}$	exp1	0.1	0.18	0.1	0.11
VH one-lepton	exp1	< 0.1	0.094	0.1	0.064
VH dilepton	exp1	< 0.1	0.080	< 0.1	0.08
$t\bar{t}H$ hadronic	exp1	0.1	0.86	0.2	0.49
$t\bar{t}H$ leptonic	exp1	< 0.1	0.10	0.2	0.28

VIII. SYSTEMATIC UNCERTAINTIES

The various types of systematic uncertainties are presented in this section according to the way they affect the determination of the signal strengths. The theoretical and experimental uncertainties on the yields of diphoton events from Higgs boson decays are discussed in Sec. VIII A. The systematic uncertainties affecting the

TABLE VII. Number of background events B_{90} in the smallest interval expected to contain 90% of the signal events S_{90} (see $N_{\rm S}$ in Tables II and III), measured by fits to the data, and the expected purity $f_{90} \equiv S_{90}/(S_{90} + B_{90})$ and signal significance $Z_{90} \equiv S_{90}/\sqrt{S_{90} + B_{90}}$ in each event category for the 7 TeV and 8 TeV data.

| Category | $\sqrt{s} = 7$ | | | $\sqrt{S} = 8$ | | |
	B_{90}	f_{90}	Z_{90}	B_{90}	f_{90}	Z_{90}
Central - low $p_{\rm Tt}$	400	0.05	1.1	2400	0.05	2.4
Central - high $p_{\rm Tt}$	11	0.14	0.52	68	0.13	1.2
Forward - low $p_{\rm Tt}$	1400	0.02	0.94	8500	0.02	2.0
Forward - high $p_{\rm Tt}$	47	0.05	0.38	280	0.05	0.84
VBF loose	6.6	0.18	0.52	44	0.16	1.2
VBF tight	0.48	0.64	0.75	6.7	0.44	1.5
VH hadronic	2.9	0.16	0.29	18	0.14	0.62
VH $E_{\rm T}^{\rm miss}$	0.95	0.21	0.23	3.2	0.24	0.49
VH one-lepton	0.24	0.55	0.40	4.4	0.26	0.63
VH dilepton	0.00	1.0	0.20	0.27	0.46	0.32
$t\bar{t}H$ hadronic	0.21	0.22	0.11	1.8	0.20	0.30
$t\bar{t}H$ leptonic	0.11	0.46	0.21	0.53	0.50	0.51

event categorization due to migrations of signal events from or to other categories are presented in Sec. VIII B. The systematic uncertainties related to the photon energy scale and resolution are reported in Sec. VIII C. The systematic uncertainties due to potential spurious signals induced by systematic differences between the background parameterization and the background component of the data are obtained with the technique described in Sec. VII B and reported in Table VI.

A. Uncertainties affecting the integrated signal yield

1. Theoretical uncertainties

The predicted total cross sections for the signal processes have uncertainties due to missing higher-order terms in the perturbative calculations of QCD processes that are estimated by varying the factorization and renormalization scales. There are additional uncertainties related to the PDFs, the strong coupling constant $\alpha_{\rm S}$, and the $H \to \gamma\gamma$ branching ratio. The uncertainties on the Higgs boson production cross sections are listed in Table VIII for $m_H = 125.4$ GeV, separately for $\sqrt{s} = 7$ TeV and $\sqrt{s} = 8$ TeV. The uncertainties estimated by varying the QCD scales affect the production processes independently, apart from WH and ZH uncertainties, which are treated as fully correlated. For the $tHbj$ and tHW production processes, the scale uncertainties are obtained by varying the renormalization and factorization scales by factors of 1/2 and 2 in the event generators (Sec. III) and the PDF uncertainties are estimated by studying the impact of the variations within the CT10 PDF set. For the other processes these uncertainties are taken from Ref. [20]. The combined uncertainties on the effective lu-

minosities for *gg*- and *qq*-initiated processes due to PDF and α_S uncertainties are independent but they affect the relevant processes coherently. Both of these sets of uncertainties affect the 7 TeV and the 8 TeV cross sections coherently. The impact of scale and PDF uncertainties on the kinematic acceptance for signal events is found to be negligible relative to the impact of the uncertainties on the cross sections. The uncertainty on the $H \to \gamma\gamma$ branching ratio for $m_H = 125.4$ GeV is $\pm 5\%$. These theoretical uncertainties, which vary only at the per mille level within 1–2 GeV of $m_H = 125.4$ GeV, are taken from Ref. [20].

TABLE VIII. Theoretical uncertainties [%] on cross sections for Higgs boson production processes for $\sqrt{s} = 7$ TeV and $\sqrt{s} = 8$ TeV for $m_H = 125.4$ GeV, as described in Sec. VIII A 1. Except for the *tHbj* and *tHW* processes, the uncertainties are taken from Ref. [20].

Process	QCD scale		PDF+α_S	
	$\sqrt{s} = 7$ TeV	$\sqrt{s} = 8$ TeV	$\sqrt{s} = 7$ TeV	$\sqrt{s} = 8$ TeV
ggF	+7.1	+7.2	+7.6	+7.5
	−7.8	−7.8	−7.1	−6.9
VBF	+0.3	+0.2	+2.5	+2.6
	−0.3	−0.2	−2.1	−2.8
WH	+1.0	+1.0	+2.6	+2.4
	−1.0	−1.0	−2.6	−2.4
ZH	+2.9	+3.1	+2.6	+2.5
	−2.9	−3.1	−2.6	−2.5
$t\bar{t}H$	+3.2	+3.8	+8.4	+8.1
	−9.3	−9.3	−8.4	−8.1
$b\bar{b}H$	+10	+10	+6.2	+6.1
	−15	−15	−6.2	−6.1
$tHbj$	+7	+6	+4	+4
	−6	−5	−4	−4
tHW	+7	+9	+10	+10
	−6	−7	−10	−10

2. Sizes of MC samples

The finite size of the MC signal samples may induce non-negligible statistical uncertainties depending on the category and the production process. The impact of these uncertainties on the individual signal strength parameters is estimated for each event category by analyzing representative MC datasets containing both Higgs boson signal and continuum background: for the signal the sample size is fixed to the one expected in data by the SM predictions, and for the background to the observed numbers of events. The uncertainties that contribute more than 0.1% in quadrature to the total expected uncertainties are retained. The 14 uncertainties that contribute more than 0.1% in quadrature to the total expected uncertainties are propagated, but their contribution is at the level of 1% or less, which is much smaller than the expected statistical uncertainties on the individual signal strengths.

3. Experimental uncertainties

The expected signal yields are affected by the experimental systematic uncertainties listed below.

1. The uncertainties on the integrated luminosities are 1.8% for the 7 TeV data and 2.8% for the 8 TeV data [104]. They are treated as uncorrelated.

2. The trigger efficiencies in data are determined by combining the results from two different measurements. The first measurement is performed with photons in $Z \to \ell\ell\gamma$ events, where ℓ is an electron or a muon. These events are collected with lepton-based triggers, making the photon candidates in these samples unbiased with respect to the trigger. The second measurement, based on the bootstrap technique described in Ref. [105], is performed on a background-corrected photon sample selected only by a first-level trigger, which has an efficiency of 100% for signal-like photons in events that pass the diphoton selection criteria (Sec. V). Both measurements are dominated by statistical uncertainties. The uncertainties on the trigger efficiencies based on these measurements are estimated to be 0.2% for both the 7 TeV and 8 TeV data and are fully uncorrelated.

3. The uncertainty on the photon identification efficiency for the 8 TeV data is derived from measurements performed with data using three different methods [80] that cover the full E_T spectrum relevant for this analysis. In the first method, the efficiency is measured in a pure and unbiased sample of photons obtained by selecting radiative $Z \to \ell\ell\gamma$ decays without using the photon identification to select the photon, and where ℓ is an electron or a muon. In the second method, the photon efficiency is measured using $Z \to ee$ data by extrapolating the properties of electron showers to photon showers using MC events [80]. In the third method, the photon efficiency is determined from a data sample of isolated photon candidates from prompt γ–jet production after subtracting the measured fraction of jet–jet background events. The combined uncertainty on the photon identification efficiency in data relative to MC simulation ranges between 0.5% and 2.0% depending on the E_T and η of the photon and on whether the photon is unconverted or converted and reconstructed with one or two tracks. For the 7 TeV data, more conservative uncertainties, ranging from 4% to 7%, are used because of the stronger correlation of the NN-based identification algorithm with the photon isolation, and because it relies more strongly on the correlations between the individual shower shape variables. Because these two effects complicate the measurement of the identification performance in data, conservative uncertainties, taken as the full difference between the ef-

ficiencies measured in data and the ones predicted by simulation, are used. The uncertainties on the signal yield due to the uncertainty on the photon identification efficiency are 8.4% for the 7 TeV data and 1.0% for the 8 TeV data and are treated as uncorrelated.

4. The uncertainty on the isolation efficiency is conservatively taken as the full size of the applied correction described in Sec. IV A. The effect on the signal yield varies among categories (depending on their photon E_T spectrum). These uncertainties, which range between 1.3% and 2.3%, are estimated with the 8 TeV dataset and are assumed to be the same in the 7 TeV data but uncorrelated between the two datasets.

The estimated values of the experimental uncertainties for both datasets are summarized in Table IX. Larger uncertainties, also shown in the table, on the photon identification and isolation selection efficiencies are assigned to the categories sensitive to $t\bar{t}H$ and VH production modes. The presence of large hadronic activity (high jet multiplicity) in these events, which is partially correlated with the photon selection and isolation efficiency, makes it difficult to measure the efficiencies precisely. The impact of these additional systematic uncertainties is, however, negligible relative to the statistical uncertainties on the measurements of $\mu_{t\bar{t}H}$, μ_{ZH}, and μ_{WH}.

TABLE IX. Relative systematic uncertainties on the inclusive yields [%] for the 7 TeV and 8 TeV data. The numbers in parentheses refer to the uncertainties applied to events in the categories that are sensitive to $t\bar{t}H$ and VH production modes. The ranges of the category-dependent uncertainties due to the isolation efficiency are reported.

Uncertainty source	$\sqrt{s} = 7$ TeV	$\sqrt{s} = 8$ TeV
Luminosity	1.8	2.8
Trigger	0.2	0.2
Photon Id.	8.4(9.3)	1.0(4.1)
Isolation	1.3–2.3(3.8)	1.3–2.3(3.8)

Finally, uncertainties on the signal yields due to the photon energy scale and primary vertex selection are found to be negligible relative to the ones discussed above.

B. Migration uncertainties

The impacts of theoretical and experimental uncertainties on the predicted contributions from the various Higgs boson production processes to each event category are summarized in the following.

1. Theory uncertainties

1. The uncertainty on the Higgs boson production cross section through gluon fusion in association with two or more jets is estimated by applying an extension of the so-called Stewart–Tackmann method [106, 107] to predictions made by the MCFM [108] generator: an uncertainty of 20% is assigned to the ggF component in the VBF loose, VBF tight, and VH hadronic categories. Since the VBF categories make use of the azimuthal angle between the diphoton and dijet systems, which is sensitive to the presence of a third jet, additional uncertainties are introduced for the ggF contribution in these categories using a technique described in Ref. [20]. These uncertainties are found to be 25% and 52% for the VBF loose and VBF tight categories, respectively.

2. The presence of additional hadronic activity from the underlying event (UE) may produce significant migrations of ggF events to the VBF and $t\bar{t}H$ hadronic categories. The uncertainties on the UE modeling are conservatively estimated as the full change in signal migration in MC simulation with and without the UE. The uncertainties are 5–6% of the 18–41% component of ggF in the VBF categories, and 60% of the 8–11% ggF contribution in the $t\bar{t}H$ hadronic category. In addition, the presence of the UE directly affects the $t\bar{t}H$ yield in the $t\bar{t}H$ hadronic and $t\bar{t}H$ leptonic categories by 11% and 3%, respectively. The differences between the uncertainties for the 7 TeV and 8 TeV data are small. Tables II and III show details of the nominal yields of the signal processes in the event categories. The impacts of these uncertainties are small compared with the statistical uncertainties on the signal strengths for these categories.

3. The uncertainty on the modeling of the p_T spectrum of the Higgs boson for the ggF process can cause migrations of events between the low and the high p_{Tt} categories. The size of the effect has been checked using the HRES2.1 prediction by varying the renormalization, factorization, and two resummation scales. The uncertainties for the high-p_{Tt} categories are estimated from the absolute values of the largest changes in the event categorization caused by the scale variations. Events in the low-p_{Tt} categories are assigned an uncertainty according to the Stewart–Tackmann procedure. The size of the effect varies among categories; it is as large as about 24% in the high-p_{Tt} categories.

4. The VBF selection uses angular variables $\Delta\phi_{jj}$ and η^* that involve the two leading jets, as discussed in Sec. VI C. The second jet in the generation of ggF events by POWHEG-BOX+PYTHIA8 predominantly comes from the parton shower generated

by PYTHIA8; therefore, the angular correlation between the two jets is not well modeled. The uncertainty due to this modeling is taken to be the difference in the event categorization caused by reweighting the events in the POWHEG-BOX sample to reproduce the p_T spectrum of the Higgs boson predicted by MINLO HJJ [64], which models the angular correlation between the first and second jet produced in gluon fusion to NLO accuracy. The mis-modeling of $\Delta\phi_{jj}$ (η^*) typically changes the number of ggF events in the VBF tight and VBF loose categories by at most 11.2% (6.6%) and 8.9% (4.8%), respectively.

5. Additional uncertainties are estimated for production processes contributing significantly to the $t\bar{t}H$ categories due to acceptance changes observed when varying the renormalization and factorization scales. The uncertainty on $t\bar{t}H$ production itself is 2% (1%) in the $t\bar{t}H$ leptonic (hadronic) category. An uncertainty of 50% is attributed to the ggF contribution in the $t\bar{t}H$ sensitive categories while an uncertainty of 4–8% is attributed to the WH, $tHbj$ and tHW contributions to account for the sensitivity of the acceptance to scale changes. The impact is independent for the three $t\bar{t}H$ and tH production processes, but coherent in the two $t\bar{t}H$ event categories and for $\sqrt{s} = 7$ TeV and 8 TeV. In addition, the uncertainties on the ggF, VBF and WH contributions to the $t\bar{t}H$ categories are assumed to be 100% to account for the uncertainty on the heavy flavor (HF) fraction in these production processes. The overall impact of these large uncertainties on $\mu_{t\bar{t}H}$ is about 10% (and much less for the other signal strength measurements), due to the small contributions from ggF, VBF and WH production to the $t\bar{t}H$ categories (Tables II and III).

2. Experimental uncertainties

The following potential sources of signal migration between categories caused by experimental effects are investigated.

1. Uncertainties related to jet and E_T^{miss} reconstruction affect the predicted distributions of signal events from the various production modes among the categories. The effect of the uncertainty on the jet energy scale, jet energy resolution and jet vertex fraction is estimated by varying individually each component of the uncertainties [109]. The effect of the E_T^{miss} energy scale and resolution uncertainty is estimated by varying independently the uncertainty in the energy scale and resolution of each type of physics object entering the calculation of E_T^{miss} as well as the uncertainty on the scale and resolution of the soft term [94]. There are 20 and 5 uncorrelated components that account for the jet-

TABLE X. Relative uncertainties [%] on the Higgs boson signal yield in each category and for each production process induced by the combined effects of the systematic uncertainties on the jet energy scale, jet energy resolution and jet vertex fraction. These uncertainties are approximately the same for the 7 TeV and the 8 TeV data.

Category	ggF	VBF	$t\bar{t}H$	$WH+ZH$
Central+Forward - low p_{Tt}	0.1	2.9	4.0	0.1
Central+Forward - high p_{Tt}	1.1	4.5	3.5	1.4
VBF loose	12	4.4	7.6	13
VBF tight	13	9.1	6.3	17
VH hadronic	2.8	4.1	9.5	2.5
VH E_T^{miss}	2.6	9.0	1.2	0.2
VH one-lepton	4.9	6.2	2.8	0.5
VH dilepton	0	0	5.1	1.0
$t\bar{t}H$ hadronic	11	21	7.3	22
$t\bar{t}H$ leptonic	37	7.7	0.5	7.4

and E_T^{miss}-related uncertainties, respectively. Tables X and XI show the impact of the jet and E_T^{miss} uncertainties. To simplify the presentation of the results, categories and processes for which each source of uncertainty has a similar impact are merged. These uncertainties are fully correlated between the 7 TeV and 8 TeV datasets.

2. The impact of the uncertainty in the b-tagging efficiency on the migration of events to and from the $t\bar{t}H$ categories is decomposed into 10 (3) independent contributions in the 8 TeV (7 TeV) data analysis. The uncertainty on the $t\bar{t}H$ yield in the $t\bar{t}H$ categories from the uncertainty on the b-tagging efficiency ranges from 1 to 3%. The uncertainties affecting other production processes that have the largest impact on the yield in the ttH categories are 20-30% of the ggF component in the hadronic category and 6-7% to the WH contribution in the leptonic channel.

3. The total impact of the lepton reconstruction, identification and isolation uncertainties on any of the selection efficiencies and event fractions of the signal production processes for the event categories in Tables II and III is found to be below 1%.

C. Impact of diphoton resolution and mass scale uncertainties on the fitted signal yield

1. Diphoton mass resolution

The precise determination of the uncertainty on the signal strengths due to the diphoton mass resolution is a key point in this analysis. It defines the range over which the signal model width is allowed to change in the fit, thus directly affecting the estimation of the number of

TABLE XI. Relative uncertainties [%] on the Higgs boson signal yield in each category and for each production process induced by systematic uncertainty on the E_T^{miss} energy scale and resolution. The uncertainties, which are approximately the same for the 7 TeV and 8 TeV data, are obtained by summing in quadrature the impacts on the signal yield of the variation of each component of the E_T^{miss} energy scale within its uncertainty.

Category	ggF+VBF	$t\bar{t}H$	WH	ZH
Untagged	0.0	0.2	0.1	0.2
VBF loose	0.0	1.0	0.1	0.2
VBF tight	0.0	2.7	1.1	0.0
VH hadronic	0.0	0.7	0.0	0.1
VH E_T^{miss}	35	1.1	1.3	0.9
VH one-lepton	4.5	0.6	0.4	4.0
VH dilepton	0.0	2.0	0.0	0.1
$t\bar{t}H$ hadronic	0.0	0.0	0.0	0.0
$t\bar{t}H$ leptonic	1.9	0.1	1.0	3.0

TABLE XII. Systematic uncertainties on the diphoton mass resolution for the 8 TeV data [%] due to the four contributions described in the text. For each category, the uncertainty is estimated by using a simulation of the Higgs boson production process which makes the largest contribution to the signal yield.

Category	Constant term	Sampling term	Material modeling	Noise term
Central - low p_{Tt}	7.5	2.6	4.9	2.6
Central - high p_{Tt}	9.6	5.6	6.2	1.7
Forward - low p_{Tt}	9.9	1.3	6.0	2.1
Forward - high p_{Tt}	12	2.8	7.8	1.9
VBF loose	9.4	2.6	6.0	2.1
VBF tight	10	3.8	6.5	2.1
VH hadronic	11	4.0	7.2	1.6
VH E_T^{miss}	11	3.6	7.4	1.7
VH one-lepton	9.8	2.8	6.3	2.1
VH dilepton	9.5	2.7	6.2	2.1
$t\bar{t}H$ hadronic	9.6	3.6	6.3	1.9
$t\bar{t}H$ leptonic	9.5	3.4	6.2	2.1

signal events. The energy resolution and its uncertainty for photons are estimated by extrapolating from the ones for electrons. The electron energy resolution and its uncertainty are measured in data using $Z \rightarrow ee$ events that, however, can only provide constraints for electrons with $p_T \simeq 40$ GeV. The extrapolation from electrons to photons and to different energy ranges relies on an accurate modeling of the resolution in the detector simulation. In the model used in this analysis, the total resolution is described in terms of four energy-dependent contributions [15]: the asymptotic resolution at high energy, i.e. the constant term; the intrinsic sampling fluctuations of the calorimeter; the effect of passive material upstream of the calorimeter; and the electronic and pileup noise. The effects on the various categories due to the the four contributions to the uncertainty in the mass resolution are summarized in Table XII for the 8 TeV data: the typical relative uncertainty on the diphoton mass resolution obtained from the sum in quadrature of these contributions is 10–15% for $m_H \simeq 125$ GeV. The uncertainties for the 7 TeV data are very similar except for the reduced size of the pileup contribution, which ranges from 0.9% to 1.4%. These four contributions are uncorrelated while each contribution affects both of the parametric width parameters σ_{CB} and σ_{GA} in the signal model (Sec. VII A) for all the categories and for both the 7 TeV and 8 TeV data coherently.

2. Diphoton mass scale

The uncertainties on the diphoton mass scale affect the position of the signal mass peak through variations of the peak of the Crystal Ball (μ_{CB}) and Gaussian (μ_{GA}) components of the signal model. The dominant systematic uncertainties on the position of the mass peak arise from uncertainties on the photon energy scale. These un-

certainties, discussed in detail in Refs. [9, 15], are propagated to the diphoton mass distribution in the signal model for each of the 12 categories. The total uncertainty on the position of the mass peak from the photon energy scale systematic uncertainties ranges from 0.18% to 0.31% depending on the category. A second contribution, varying from 0.02% to 0.31%, comes from the choice of the background model and is evaluated using the technique presented in Ref. [9]. Finally, the systematic uncertainty on the mass scale related to the reconstruction of the diphoton vertex is estimated to be 0.03% for all the categories. As discussed in Sec. X, the uncertainty on the diphoton mass scale is expected to flatten the dependence of μ as a function of m_H in the region around the true value of m_H.

IX. STATISTICAL PROCEDURE

The data are interpreted following the statistical procedure summarized in Ref. [102] and described in detail in Ref. [110]. An extended likelihood function is built from the number of observed events and analytic functions describing the distributions of $m_{\gamma\gamma}$ in the range 105–160 GeV for the signal (see Sec. VII A) and the background (see Sec. VII B).

The likelihood for a given category c is a marked Poisson probability distribution,

$$\mathcal{L}_c = \text{Pois}(n_c|N_c(\boldsymbol{\theta})) \cdot \prod_{i=1}^{n_c} f_c(m_{\gamma\gamma}^i, \boldsymbol{\theta}) \cdot G(\boldsymbol{\theta}),$$

where n_c is the number of candidates, N_c is the expected number of candidates, $f_c(m_{\gamma\gamma}^i)$ is the value of the probability density function (pdf) of the invariant mass dis-

tribution evaluated for each candidate i, $\boldsymbol{\theta}$ are nuisance parameters and $G(\boldsymbol{\theta})$ is a set of unit Gaussian constraints on certain of the nuisance parameters, as described in the following.

The number of expected candidates is the sum of the hypothesized number of signal events plus the fitted number of background candidates, $N_{\mathrm{bkg},c}$, and the fitted spurious signal, $N_{\mathrm{spur},c} \cdot \theta_{\mathrm{spur},c}$,

$$N_c = \mu \cdot N_{\mathrm{S},c}(\boldsymbol{\theta}_c^{\mathrm{yield}}, \boldsymbol{\theta}_c^{\mathrm{migr}}, m_H) + N_{\mathrm{bkg},c} + N_{\mathrm{spur},c} \cdot \theta_{\mathrm{spur},c},$$

where $N_{\mathrm{S},c}(\boldsymbol{\theta}_c^{\mathrm{yield}}, \boldsymbol{\theta}_c^{\mathrm{migr}}, m_H)$ is the number of signal events predicted by the SM from all production processes, $\boldsymbol{\theta}_c^{\mathrm{yield}}$ and $\boldsymbol{\theta}_c^{\mathrm{migr}}$ are the nuisance parameters that implement the systematic uncertainties affecting the yields of the Higgs boson production (Sec. VIII A) in and migration between the 12 categories (Sec. VIII B), respectively. In more detail, the invariant mass distribution for each category has signal and background components,

$$f_c(m_{\gamma\gamma}^i) = [(\mu \cdot N_{\mathrm{S},c} + N_{\mathrm{spur},c} \cdot \theta_{\mathrm{spur},c}) \cdot f_{\mathrm{S},c}(m_{\gamma\gamma}^i, \boldsymbol{\theta}_{\mathrm{S},c}^{\mathrm{shape}}) + N_{\mathrm{bkg},c} \cdot f_{\mathrm{bkg},c}(m_{\gamma\gamma}^i, \boldsymbol{\theta}_{\mathrm{bkg},c}^{\mathrm{shape}})]/N_c,$$

where $\boldsymbol{\theta}_{\mathrm{S},c}^{\mathrm{shape}}$ and $\boldsymbol{\theta}_{\mathrm{bkg},c}^{\mathrm{shape}}$ are nuisance parameters associated with systematic uncertainties affecting the resolutions (Sec. VIII C 1) and positions (Sec. VIII C 2) of the invariant mass distributions of the signal $f_{\mathrm{S},c}$ (described in Sec. VII A) and background $f_{\mathrm{bkg},c}$ (described in Sec. VII B), respectively.

Apart from the spurious signal, systematic uncertainties are incorporated into the likelihood by multiplying the relevant parameter of the statistical model by a factor

$$F_{\mathrm{G}}(\sigma, \theta) = (1 + \sigma \cdot \theta) \tag{3}$$

in the case of a Gaussian pdf for the effect of an uncertainty of size σ or, for cases where a negative model parameter does not make physical sense (e.g. the uncertainty on a measured integrated luminosity),

$$F_{\mathrm{LN}}(\sigma, \theta) = e^{\sqrt{\ln(1+\sigma^2)}\theta} \tag{4}$$

for a log-normal pdf. In both cases the corresponding component of the constraint product $G(\theta)$ is a unit Gaussian centered at zero for θ. The systematic uncertainties affecting the yield and mass resolution use the log-normal form while a Gaussian form is used for all others. When two uncertainties are considered fully correlated they share the same nuisance parameter θ with different values of σ. Systematic uncertainties with partial correlations are decomposed into their uncorrelated and fully correlated components before being assigned to nuisance parameters.

The likelihood for the combined signal strength is the product of 24 likelihoods, consisting of the 12 category likelihoods for each dataset (7 TeV and 8 TeV). The combined signal strength and its uncertainty are determined

with the profile likelihood ratio test statistic

$$\lambda(\mu) = -2 \ln \frac{\mathcal{L}(\mu, \hat{\hat{\boldsymbol{\theta}}}_\mu)}{\mathcal{L}(\hat{\mu}, \hat{\boldsymbol{\theta}})}, \tag{5}$$

where $\hat{\mu}$ and $\hat{\boldsymbol{\theta}}$ are the values of the combined signal strength and nuisance parameters that unconditionally maximize the likelihood while $\hat{\hat{\boldsymbol{\theta}}}_\mu$ are the values of the nuisance parameters that maximize the likelihood on the condition that μ is held fixed to a given value. In the asymptotic approximation, which is valid for all the results presented here, $\lambda(\mu)$ may be interpreted as a change in χ^2 with respect to the minimum [102] such that approximate confidence intervals are easily constructed.

A summary of the different sources of systematic uncertainty, the number of associated nuisance parameters and the functional forms used as constraints is reported in Table XIII. As can be seen in Table XIII there are 146 constrained nuisance parameters associated with systematic uncertainties. Twelve of these are associated with the spurious signal in each of the 12 event categories. There are 49 unconstrained nuisance parameters that describe the normalizations and shapes of the fitted backgrounds in the 12 categories for the 7 TeV and 8 TeV data. As at least 2 events are needed to constrain the slope of the exponential background model, the categories with low expected yields are assumed to have the same shape parameters for the 7 TeV and the 8 TeV data. The $VH\,E_{\mathrm{T}}^{\mathrm{miss}}$, one-lepton, and dilepton categories are defined to have low yield since the probabilities to observe 2 events in the 7 TeV data are less than 1% based on the numbers of events observed in the corresponding 8 TeV data categories.

To test the signal strengths of individual production processes or groups of them, the hypothesized number of signal events and invariant mass distribution are decomposed into individual contributions,

$$\mu N_{\mathrm{S},c} \to \sum_p \mu_p N_{p,c}, \tag{6}$$

where μ_p is the hypothesized signal strength for production process $p \in \{\mathrm{ggF}, \mathrm{VBF}, ZH, WH, t\bar{t}H, b\bar{b}H, tH\}$ and $N_{p,c}$ is the number of signal events predicted by the SM in category c for production process p (the nuisance parameters are not shown in Eq. (6), but they follow the decomposition). In several of the results in the next section some of the signal strengths are required to have the same value, such as for the measurement of the combined signal strength where all seven are set equal. For the measurements of individual signal strengths and signal strength ratios, $\mu_{b\bar{b}H}$ and μ_{tH} are held constant at 1, thus treating them effectively as backgrounds.

The total uncertainty $^{+\delta\mu_+}_{-\delta\mu_-}$ at the 68% confidence level (CL) of a measured signal strength μ_{X} with best fit value $\hat{\mu}_{\mathrm{X}}$ is estimated by finding the points where $\Lambda(\hat{\mu}_{\mathrm{X}} + \delta\mu_+) = \Lambda(\hat{\mu}_{\mathrm{X}} - \delta\mu_-) = 1$. The statistical component of the total uncertainty is estimated by fixing

TABLE XIII. Summary of sources of systematic uncertainty σ, the number of nuisance parameters N_{NP} used to implement them for the combination of the 7 TeV and 8 TeV data (i is the index to each of the unique nuisance parameters θ), the factor in the likelihood function $F_{\mathrm{G}}(\sigma, \theta)$ or $F_{\mathrm{LN}}(\sigma, \theta)$ (defined in Eqs. (3) and (4)) that implements their impact on signal yields, mass resolution and scale, and the spurious signals resulting from the background parameterization, and the section in which they are presented. When acting on $N_{\mathrm{S}}^{\mathrm{tot}}$ the uncertainty value is the same for all processes, whereas the uncertainty has a different value for each signal process for the case denoted N_{S}^{p}.

		Syst. source	N_{NP}	Implementation	Section
Yield	Theory	Scales	7	$N_{\mathrm{S}}^{p}\,F_{\mathrm{LN}}(\sigma_i, \theta_i)$	VIII A 1
		PDF+α_{S}	2	$N_{\mathrm{S}}^{p}\,F_{\mathrm{LN}}(\sigma_i, \theta_i)$	VIII A 1
		Br. ratio	1	$N_{\mathrm{S}}^{\mathrm{tot}}\,F_{\mathrm{LN}}(\sigma_i, \theta_i)$	VIII A 1
	Exp.	Luminosity	2	$N_{\mathrm{S}}^{\mathrm{tot}}\,F_{\mathrm{LN}}(\sigma_i, \theta_i)$	VIII A 3.1
		Trigger	2	$N_{\mathrm{S}}^{\mathrm{tot}}\,F_{\mathrm{LN}}(\sigma_i, \theta_i)$	VIII A 3.2
		Photon ID	2	$N_{\mathrm{S}}^{p}\,F_{\mathrm{LN}}(\sigma_i, \theta_i)$	VIII A 3.3
		Isolation	2	$N_{\mathrm{S}}^{p}\,F_{\mathrm{LN}}(\sigma_i, \theta_i)$	VIII A 3.4
MC		MC stats.	14	$N_{\mathrm{S}}^{p}\,F_{\mathrm{G}}(\sigma_i^{p}, \theta_i)$	VIII A 2
Migrations	Theory	Jet-bin	2	$N_{\mathrm{S}}^{\mathrm{ggF}}\,F_{\mathrm{LN}}(\sigma_i^{\mathrm{ggF}}, \theta_i^{\mathrm{ggF}})$	VIII B 1.1
		UE+PS	1	$N_{\mathrm{S}}^{p}\,F_{\mathrm{G}}(\sigma_i^{p}, \theta_i)$	VIII B 1.2
		Higgs p_{T}	1	$N_{\mathrm{S}}^{\mathrm{ggF}}\,F_{\mathrm{G}}(\sigma_i^{\mathrm{ggF}}, \theta_i^{\mathrm{ggF}})$	VIII B 1.3
		$\Delta\phi_{jj}$	1	$N_{\mathrm{S}}^{\mathrm{ggF}}\,F_{\mathrm{LN}}(\sigma_i^{\mathrm{ggF}}, \theta_i^{\mathrm{ggF}})$	VIII B 1.4
		η^{*}	1	$N_{\mathrm{S}}^{\mathrm{ggF}}\,F_{\mathrm{LN}}(\sigma_i^{\mathrm{ggF}}, \theta_i^{\mathrm{ggF}})$	VIII B 1.4
		$t\bar{t}H$ model	2	$N_{\mathrm{S}}^{t\bar{t}H}\,F_{\mathrm{LN}}(\sigma_i^{t\bar{t}H}, \theta_i^{t\bar{t}H})$	VIII B 1.5
		HF content	1	$N_{\mathrm{S}}^{p}\,F_{\mathrm{LN}}(\sigma_i^{p}, \theta_i)$	VIII B 1.5
		Scale ($t\bar{t}H$ cat.)	4	$N_{\mathrm{S}}^{p}\,F_{\mathrm{LN}}(\sigma_i^{t\bar{t}H}, \theta_i^{t\bar{t}H})$	VIII B 1.5
	Exp.	Jet reco.	20	$N_{\mathrm{S}}^{p}\,F_{\mathrm{G}}(\sigma_i^{p}, \theta_i)$	VIII B 2.1
		$E_{\mathrm{T}}^{\mathrm{miss}}$	5	$N_{\mathrm{S}}^{p}\,F_{\mathrm{G}}(\sigma_i^{p}, \theta_i)$	VIII B 2.1
		b-tagging	13	$N_{\mathrm{S}}^{p}\,F_{\mathrm{G}}(\sigma_i^{p}, \theta_i)$	VIII B 2.2
		Lepton ID+isol.	2	$N_{\mathrm{S}}^{p}\,F_{\mathrm{G}}(\sigma_i^{p}, \theta_i)$	VIII B 2.3
		Lepton isolation	2	$N_{\mathrm{S}}^{p}\,F_{\mathrm{G}}(\sigma_i^{p}, \theta_i)$	VIII B 2.3
Mass		Resolution	4	$\sigma_{\mathrm{CB}}\,F_{\mathrm{LN}}(\sigma_i, \theta_i)$ $\sigma_{\mathrm{GA}}\,F_{\mathrm{LN}}(\sigma_i, \theta_i)$	VIII C 1
		Scale	43	$\mu_{\mathrm{CB}}\,F_{\mathrm{G}}(\sigma_i, \theta_i)$ $\mu_{\mathrm{GA}}\,F_{\mathrm{G}}(\sigma_i, \theta_i)$	VIII C 2
Back.		Spurious signal	12	$N_{\mathrm{spur},c}\,\theta_{\mathrm{spur},c}$	VII B

all the 146 constrained nuisance parameters associated with systematic uncertainties summarised in Table XIII to their maximum likelihood values and finding the new points where $\Lambda_{\mathrm{stat.}}(\mu_{\mathrm{X}}) = 1$. The total systematic uncertainty is given by the quadratic difference between the total and statistical uncertainties. The separate contributions of the total experimental and total theoretical uncertainties are estimated by finding the points where $\Lambda_{\mathrm{stat.}\oplus\mathrm{expt.}}(\mu_{\mathrm{X}}) = 1$ and $\Lambda_{\mathrm{stat.}\oplus\mathrm{theory}}(\mu_{\mathrm{X}}) = 1$, re-

spectively, when fixing the 123 (23) constrained nuisance parameters associated with experimental (theoretical) uncertainty to their maximum likelihood values, and subtracting the resulting uncertainties in quadrature from the total uncertainty. For cases where the confidence intervals are approximately symmetric around the best fit value of μ_{X}, the positive and negative uncertainty contributions are reported as a single value $\pm\delta\mu$.

X. RESULTS

The observed diphoton invariant mass distribution for the sum of the 7 TeV and 8 TeV data is shown in Fig. 13 and in Fig. 14 for the sums of categories most sensitive to different production modes. In all cases, for illustration purposes, each event is weighted according to the expected signal-to-background ratio S_{90}/B_{90} for the relevant category and center-of-mass energy. The results of signal plus background fits to these spectra with m_H set to 125.4 GeV are shown together with the separate signal and background components. Both the signal plus background and background-only curves reported here are obtained from the sum of the individual curves in each category weighted in the same way as the data points.

The signal strengths are measured with the extended likelihood analysis described in Sec. IX. The profile of the negative log-likelihood ratio $\lambda(\mu)$ (Eq. (5)) of the combined signal strength μ for $m_H = 125.4$ GeV is shown in Fig. 15. The local significance Z of the observed combined excess of events, given by $\sqrt{\lambda(0)}$, is $5.2\,\sigma$ ($4.6\,\sigma$ expected). The best fit value of μ, determined by the minimum of $\lambda(\mu)$, is found to be

$$\mu = 1.17 \pm 0.23\,(\mathrm{stat.})\,{}^{+0.10}_{-0.08}\,(\mathrm{syst.})\,{}^{+0.12}_{-0.08}\,(\mathrm{theory})$$
$$= 1.17 \pm 0.27,$$

corresponding to a $0.7\,\sigma$ compatibility with the SM prediction ($\mu = 1$). Figure 16 shows the best fit value of μ as a function of m_H when mass scale systematic uncertainties are included in or excluded from the fit. The figure illustrates that when the mass scale systematic uncertainties are taken into account, the mass region compatible with the peak position is broadened. Only a slight dependence of μ on m_H in the region compatible with the value of the Higgs boson mass measured by ATLAS $m_H = 125.4 \pm 0.4$ GeV is seen. This is also a consequence of the small variation of the cross section times branching ratio versus m_H in the same region (about 2%/GeV).

The signal strengths measured in the individual event categories are shown in Fig. 17. The signal strengths measured in the four production mode–based groups of categories described in Sec. VI are presented in Fig. 18. All of these individual and grouped signal strengths are compatible with the combined signal strength.

The impacts of the main sources of systematic uncertainty presented in Sec. VIII on the combined signal strength parameter measurement are presented in
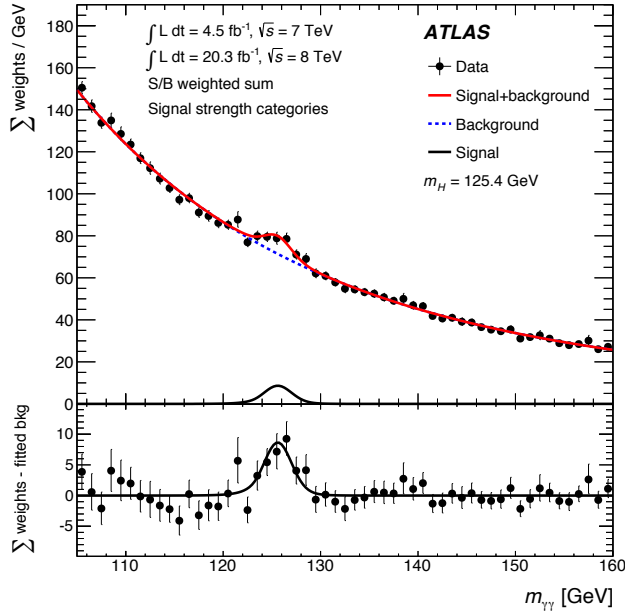
TABLE XIV. Main systematic uncertainties $\sigma_\mu^{\text{syst.}}$ on the combined signal strength parameter μ. The values for each group of uncertainties are determined by subtracting in quadrature from the total uncertainty the change in the 68% CL range on μ when the corresponding nuisance parameters are fixed to their best fit values. The experimental uncertainty on the yield does not include the luminosity contribution, which is accounted for separately.

Uncertainty group	$\sigma_\mu^{\text{syst.}}$
Theory (yield)	0.09
Experimental (yield)	0.02
Luminosity	0.03
MC statistics	< 0.01
Theory (migrations)	0.03
Experimental (migrations)	0.02
Resolution	0.07
Mass scale	0.02
Background shape	0.02

FIG. 13. Diphoton invariant mass $m_{\gamma\gamma}$ spectrum observed in the sum of the 7 TeV and 8 TeV data. Each event is weighted by the signal-to-background ratio in the dataset and category it belongs to. The errors bars represent 68% confidence intervals of the weighted sums. The solid red curve shows the fitted signal plus background model when the Higgs boson mass is fixed at 125.4 GeV. The background component of the fit is shown with the dotted blue curve. The signal component of the fit is shown with the solid black curve. Both the signal plus background and background-only curves reported here are obtained from the sum of the individual curves in each category weighted by their signal-to-background ratio. The bottom plot shows the data relative to the background component of the fitted model.

Table XIV. They are determined from the difference in quadrature between the nominal uncertainty and change in the 68% CL range on μ when the corresponding nuisance parameters are fixed to their best fit values. The sums of the squares of the theoretical uncertainties linked to the QCD scales, PDFs, and $H \to \gamma\gamma$ branching ratio account for approximately 50% of the square of the total systematic uncertainty. The dominant experimental uncertainty is from the photon energy resolution, which represents approximately 30% of the total systematic uncertainty (as above in terms of its contribution to the square of the total systematic uncertainty). In the fit to extract the signal strengths, the post-fit values of the most relevant nuisance parameters (those apart from the ones of the background model), do not show significant deviations from their pre-fit input values.

The compatibility of the combined signal strength presented in this article with the one published in Ref. [13], $\mu = 1.55 \, ^{+0.33}_{-0.28}$, is investigated using a jackknife resampling technique [111, 112] in which variances and covariances of observables are estimated with a series of sub-samples of the observations. The datasets used in the two analyses are highly correlated: 142681 events are selected in Ref. [13], 111791 events are selected in the current analysis, and 104407 events are selected in both analyses. The significance of the 0.4 difference between the combined signal strengths, including the effect of the 74% correlation between the two measurements, is calculated by applying the jackknife technique to the union of the two datasets and is found to be $2.3\,\sigma$. An uncertainty of $0.1\,\sigma$ on the compatibility between the two measurements is estimated by varying the size of the jackknife sub-samples. The decrease in the observed signal significance ($5.2\,\sigma$) with respect to the one published in Ref. [13] ($7.4\,\sigma$) is related to the reduction of the measured signal strength according to the asymptotic formula $Z = \mu/\sigma_\mu^{\text{stat}}$, where σ_μ^{stat} is the statistical component of the uncertainty on μ. In other words, the observed reductions of the significance and signal strength are consistent with each other and consistent with a statistical fluctuation at the level of $\sim 2.3\,\sigma$.

As can be seen in Figs. 17 and 18, the observed signal strengths of the tagged categories, which are dominated by production processes other than ggF, tend to be lower than the signal strengths measured with the untagged categories, which are dominated by ggF production. This tendency, combined with the optimized sensitivity of this analysis to production processes other than ggF, results in a lower combined signal strength than those measured using alternative analyses of the same dataset (or where the datasets are largely overlapping) that are inclusive with respect to the production process. The compatibility of the combined signal strength obtained in this analysis with the signal strength $\mu = 1.29 \pm 0.30$ obtained in the mass measurement analysis quoted in Ref. [9] for the diphoton channel (where the diphoton events are sorted into categories that de-
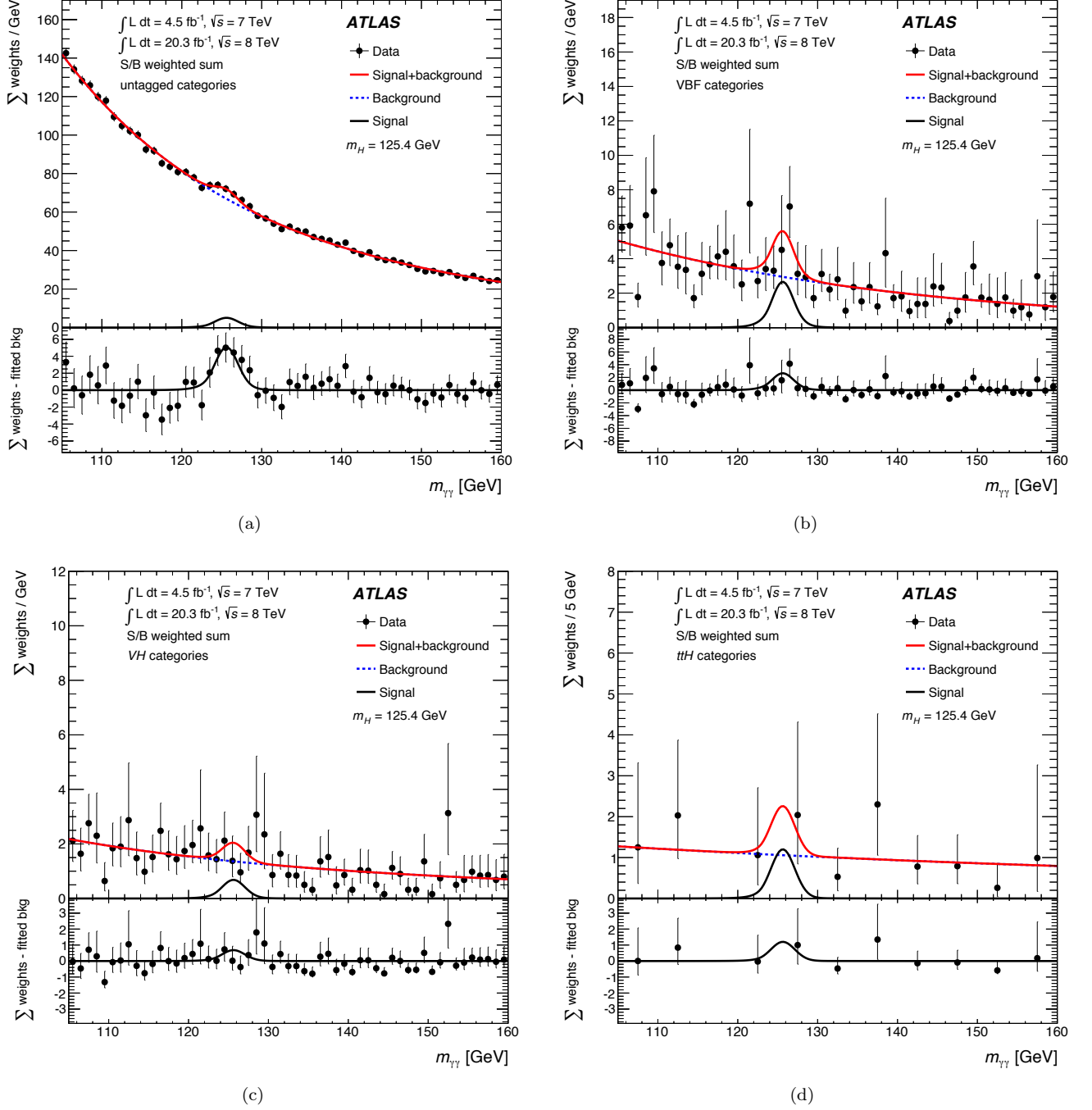
FIG. 14. Diphoton invariant mass spectra observed in the 7 TeV and 8 TeV data in four groups of categories: (a) untagged categories, which are dominated by ggF, (b) VBF categories, (c) VH and (d) $t\bar{t}H$ categories. In each plot the contribution from the different categories in each group is weighted according to the S/B ratio in each category. The errors bars represent 68% confidence intervals of the weighted sums. The solid red line shows the fitted signal plus background model when the Higgs boson mass is fixed at $m_H = 125.4$ GeV. The background component of each fit is shown with a dotted blue line. Both the signal plus background and background-only curves reported here are obtained from the sum of the individual curves in each category weighted by their signal-to-background ratio. The bottom plot in each figure shows the data relative to the background component of the fitted model.
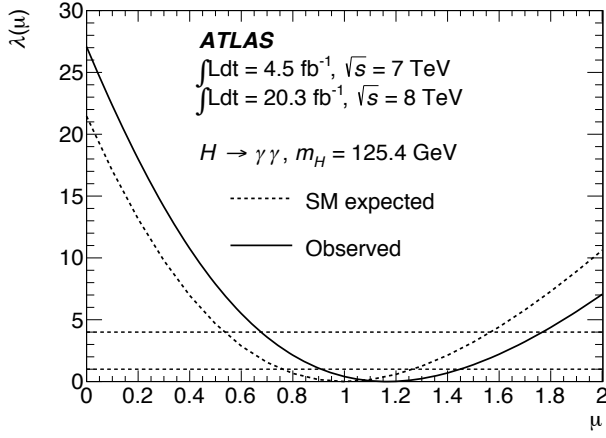
FIG. 15. The profile of the negative log-likelihood ratio $\lambda(\mu)$ of the combined signal strength μ for $m_H = 125.4$ GeV. The observed result is shown by the solid curve, the expectation for the SM by the dashed curve. The intersections of the solid and dashed curves with the horizontal dashed line at $\lambda(\mu) = 1$ indicate the 68% confidence intervals of the observed and expected results, respectively.
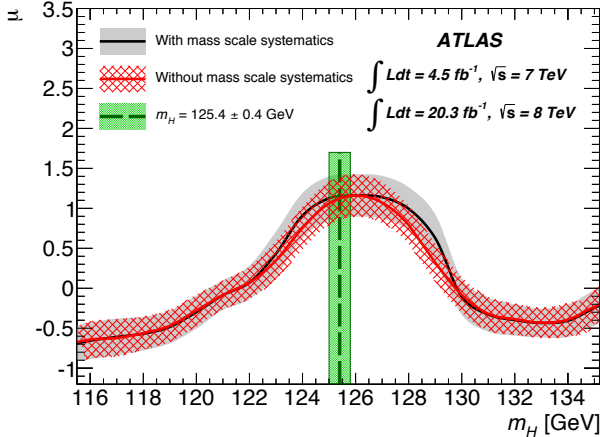
FIG. 16. The combined signal strength parameter μ versus m_H with mass scale systematic uncertainties included (black curve) and excluded (red curve). The uncertainties on the measured μ are shown as gray (red) bands with the mass scale systematic uncertainties included (excluded). The vertical dotted line and shaded band indicate the value $m_H = 125.4 \pm 0.4$ GeV.

pend only on the properties of the photons) is evaluated with the same resampling technique described above and found to be within one standard deviation. A measurement of the fiducial cross section of Higgs boson production in the $H \rightarrow \gamma\gamma$ decay channel with the ATLAS detector is performed in Ref. [113]. In order to make that analysis more model-independent, there is no use of production process–related event categories. The signal strength of the measured fiducial cross section, using
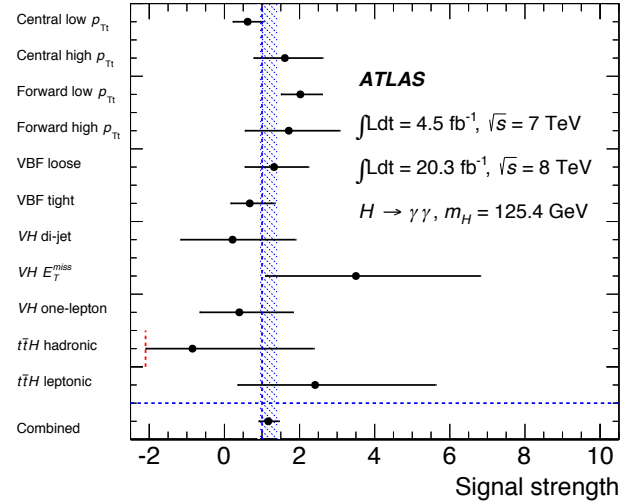
FIG. 17. The signal strength for a Higgs boson of mass $m_H = 125.4$ GeV decaying via $H \rightarrow \gamma\gamma$ as measured in the individual analysis categories, and the combined signal strength, for the combination of the 7 TeV and 8 TeV data. The vertical hatched band indicates the 68% confidence interval of the combined signal strength. The vertical dashed line at signal strength 1 indicates the SM expectation. The vertical dashed red line indicates the limit below which the fitted signal plus background mass distribution for the $t\bar{t}H$ hadronic category becomes negative for some mass in the fit range. The VH dilepton category is not shown because with only two events in the combined sample, the fit results are not meaningful.

only the 8 TeV data, is approximately 1.4 and found to be compatible with the combined signal strength measured here within $1.2\,\sigma$ (using again the jackknife resampling technique).

In addition to the combined signal strength, the signal strengths of the primary production processes are determined by exploiting the sensitivities of the analysis categories to specific production processes, and found to be (see also Fig. 19):

$$\mu_{\text{ggF}} = 1.32 \ \pm 0.32 \ (\text{stat.}) \ ^{+0.13}_{-0.09} \ (\text{syst.}) \ ^{+0.19}_{-0.11} \ (\text{theory})$$
$$= 1.32 \pm 0.38,$$
$$\mu_{\text{VBF}} = 0.8 \ \pm 0.7 \ (\text{stat.}) \ ^{+0.2}_{-0.1} \ (\text{syst.}) \ ^{+0.2}_{-0.3} \ (\text{theory})$$
$$= 0.8 \pm 0.7,$$
$$\mu_{WH} = 1.0 \pm 1.5 \ (\text{stat.}) \ ^{+0.3}_{-0.1} \ (\text{syst.}) \ ^{+0.2}_{-0.1} \ (\text{theory})$$
$$= 1.0 \pm 1.6,$$
$$\mu_{ZH} = 0.1 \ ^{+3.6}_{-0.1} \ (\text{stat.}) \ ^{+0.7}_{-0.0} \ (\text{syst.}) \ ^{+0.1}_{-0.0} \ (\text{theory})$$
$$= 0.1 \ ^{+3.7}_{-0.1},$$
$$\mu_{t\bar{t}H} = 1.6 \ ^{+2.6}_{-1.8} \ (\text{stat.}) \ ^{+0.6}_{-0.4} \ (\text{syst.}) \ ^{+0.5}_{-0.2} \ (\text{theory})$$
$$= 1.6 \ ^{+2.7}_{-1.8}.$$

In this measurement, both μ_{tH} and $\mu_{b\bar{b}H}$ are fixed to the SM expectations ($\mu_{tH}=1$ and $\mu_{b\bar{b}H}=1$). The corre-
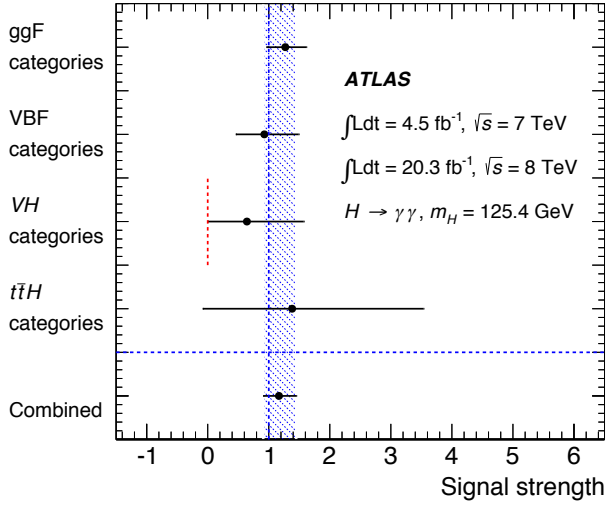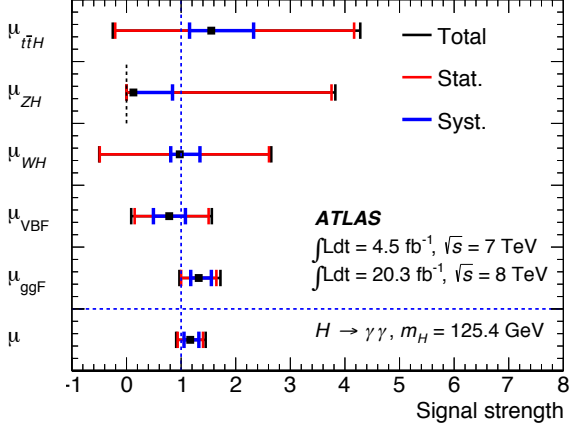
FIG. 18. The signal strength for a Higgs boson of mass $m_H = 125.4$ GeV decaying via $H \to \gamma\gamma$ as measured in groups of categories sensitive to individual production modes, and the combined signal strength, for the combination of the 7 TeV and 8 TeV data. The vertical hatched band indicates the 68% confidence interval of the combined signal strength. The vertical dashed line at signal strength 1 indicates the SM expectation. The vertical dashed red line indicates the limit below which the fitted signal plus background mass distribution for the combination of the VH categories becomes negative for some mass in the fit range.

FIG. 19. Measured signal strengths, for a Higgs boson of mass $m_H = 125.4$ GeV decaying via $H \to \gamma\gamma$, of the different Higgs boson production modes and the combined signal strength μ obtained with the combination of the 7 TeV and 8 TeV data. The vertical dashed line at $\mu = 1$ indicates the SM expectation. The vertical dashed line at the left end of the μ_{ZH} result indicates the limit below which the fitted signal plus background mass distribution becomes negative for some mass in the fit range.

lation between the fitted values of μ_{ggF} and μ_{VBF} has

been studied by still fixing both μ_{tH} and $\mu_{b\bar{b}H}$ to 1 and profiling[3] the remaining signal strengths μ_{ZH}, μ_{WH}, and $\mu_{t\bar{t}H}$. The best-fit values of μ_{ggF} and μ_{VBF} and the 68% and 95% CL contours are shown in Fig. 20.
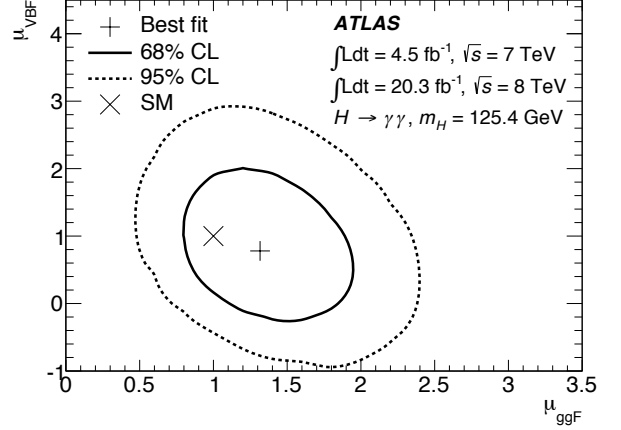
FIG. 20. The two-dimensional best-fit value of $(\mu_{\mathrm{VBF}}, \mu_{\mathrm{ggF}})$ for a Higgs boson of mass $m_H = 125.4$ GeV decaying via $H \to \gamma\gamma$ when fixing both μ_{tH} and $\mu_{b\bar{b}H}$ to 1 and profiling all the other signal strength parameters. The 68% and 95% CL contours are shown with the solid and dashed lines, respectively. The result is obtained for $m_H = 125.4$ GeV and the combination of the 7 TeV and 8 TeV data.

Compared with the measured $t\bar{t}H$ signal strength parameter $\mu_{t\bar{t}H} = 1.3 \, ^{+2.5}_{-1.7}$ (stat.) $^{+0.8}_{-0.4}$ (syst.) in Ref. [96], $\mu_{t\bar{t}H}$ measured in this analysis profits from the contribution of $t\bar{t}H$ events in other categories such as $VH \, E_{\mathrm{T}}^{\mathrm{miss}}$ and VH one-lepton. In addition, in this measurement the other contributions to the signal strength are profiled, whereas they are fixed at the SM predictions in Ref. [96].

As mentioned in the introduction, in order to test the production through VBF and associated production with a W or Z boson or a $t\bar{t}$ pair, independently of the $H \to \gamma\gamma$ branching ratio, the ratios $\mu_{\mathrm{VBF}}/\mu_{\mathrm{ggF}}$, $\mu_{VH}/\mu_{\mathrm{ggF}}$, and $\mu_{t\bar{t}H}/\mu_{\mathrm{ggF}}$ are fitted separately by fixing μ_{tH} and $\mu_{b\bar{b}H}$ to 1 and profiling the remaining signal strengths. The measured ratios

$$\mu_{\mathrm{VBF}}/\mu_{\mathrm{ggF}} = 0.6 \, ^{+0.8}_{-0.5},$$
$$\mu_{VH}/\mu_{\mathrm{ggF}} = 0.6 \, ^{+1.1}_{-0.6},$$
$$\mu_{t\bar{t}H}/\mu_{\mathrm{ggF}} = 1.2 \, ^{+2.2}_{-1.4},$$

although not significantly different from zero, are consistent with the SM predictions of 1.0. Likelihood scans of these ratios are presented in

---

[3] Profiling here means maximizing the likelihood with respect to all parameters apart from the parameters of interest μ_{ggF} and μ_{VBF}.

Fig. 21. The result for $\mu_{\rm VBF}/\mu_{\rm ggF}$ is consistent with $\mu_{{\rm VBF}+VH}/\mu_{{\rm ggF}+t\bar{t}H} = 1.1^{+0.9}_{-0.5}$ reported by ATLAS with the same data in Ref. [13], although they are not directly comparable.
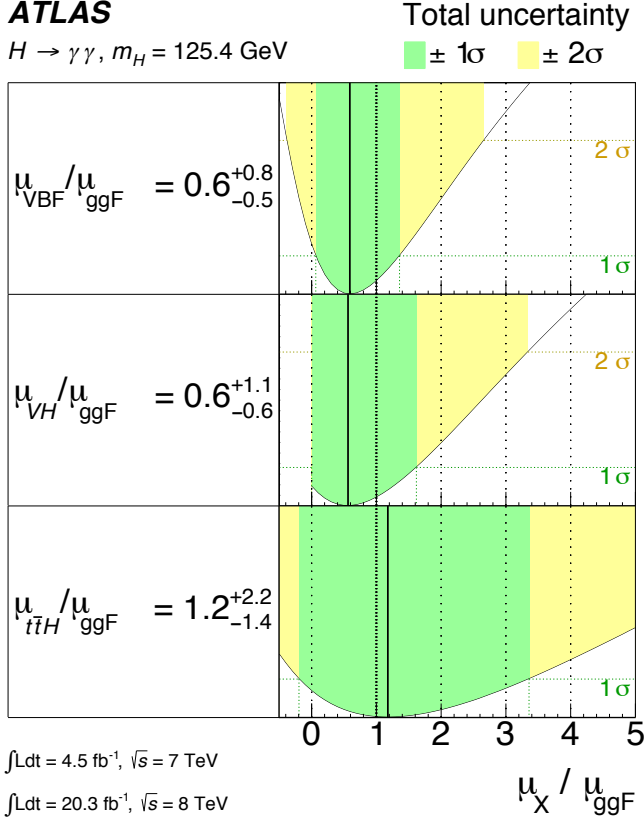

ATLAS   Total uncertainty

$H \to \gamma\gamma$, $m_H = 125.4$ GeV

$\pm 1\sigma$ $\pm 2\sigma$

$\mu_{\rm VBF}/\mu_{\rm ggF} = 0.6^{+0.8}_{-0.5}$

$\mu_{VH}/\mu_{\rm ggF} = 0.6^{+1.1}_{-0.6}$

$\mu_{t\bar{t}H}/\mu_{\rm ggF} = 1.2^{+2.2}_{-1.4}$

$\int L dt = 4.5$ fb^{-1}, $\sqrt{s} = 7$ TeV

$\int L dt = 20.3$ fb^{-1}, $\sqrt{s} = 8$ TeV

$\mu_X / \mu_{\rm ggF}$

FIG. 21. Measurements of the $\mu_{\rm VBF}/\mu_{\rm ggF}$, $\mu_{VH}/\mu_{\rm ggF}$ and $\mu_{t\bar{t}H}/\mu_{\rm ggF}$ ratios and their total errors for a Higgs boson mass $m_H = 125.4$ GeV. For a more complete illustration, the log-likelihood curves from which the total uncertainties are extracted are also shown: the best fit values are represented by the solid vertical lines, with the total $\pm 1\sigma$ and $\pm 2\sigma$ uncertainties indicated by the dark- and light-shaded band, respectively. The likelihood curve and uncertainty bands for $\mu_{VH}/\mu_{\rm ggF}$ stop at zero because below this the hypothesized signal plus background mass distribution in the VH dilepton channel becomes negative (unphysical) for some mass in the fit range.

XI. CONCLUSION

A refined measurement of Higgs boson signal strengths in the $H \to \gamma\gamma$ decay channel is performed using the proton-proton collision data recorded by the ATLAS experiment at the CERN Large Hadron Collider at center-of-mass energies of $\sqrt{s} = 7$ TeV and $\sqrt{s} = 8$ TeV corresponding to a total integrated luminosity of 25 fb^{-1} (the

LHC Run 1 dataset). The results are based on improved calibrations for photons, electrons and muons and on improved analysis techniques with respect to the previously published analysis of the same dataset. The strength of the signal relative to the SM expectation, measured at the combined ATLAS Higgs boson mass $m_H = 125.4$ GeV is found to be

$$\mu = 1.17 \pm 0.27.$$

The compatibility with the SM prediction of $\mu = 1$ corresponds to $0.7\,\sigma$. Signal strengths of the main production modes are measured separately by exploiting event categories that are designed to be sensitive to particular production modes. They are found to be

$$\mu_{\rm ggF} = 1.32 \pm 0.38,$$
$$\mu_{\rm VBF} = 0.8 \pm 0.7,$$
$$\mu_{WH} = 1.0 \pm 1.6,$$
$$\mu_{ZH} = 0.1^{+3.7}_{-0.1},$$
$$\mu_{t\bar{t}H} = 1.6^{+2.7}_{-1.8},$$

where the statistical, systematic and theoretical uncertainties are combined. The total uncertainty of both the combined and the five individual signal strength parameters presented above is dominated by the statistical uncertainty. These are the first results obtained by ATLAS in the diphoton final state for these five production mechanisms simultaneously. No significant deviations from the SM expectations are observed. More data are needed to establish evidence for Higgs boson production in the $H \to \gamma\gamma$ decay channel via the VBF, WH, ZH, and $t\bar{t}H$ production mechanisms individually. These results supersede the previous ones and represent the new reference for the signal strengths of Higgs boson production in the $H \to \gamma\gamma$ decay channel measured by ATLAS with the LHC Run 1 data.

[1] ATLAS Collaboration, Phys. Lett. B **716**, 1 (2012), arXiv:1207.7214 [hep-ex].

[2] CMS Collaboration, Phys. Lett. B **716**, 30 (2012), arXiv:1207.7235 [hep-ex].

[3] F. Englert and R. Brout, Phys. Rev. Lett. **13**, 321 (1964).

[4] P. W. Higgs, Phys. Lett. **12**, 132 (1964).

[5] P. W. Higgs, Phys. Rev. Lett. **13**, 508 (1964).

[6] G. Guralnik, C. Hagen, and T. Kibble, Phys. Rev. Lett. **13**, 585 (1964).

[7] P. W. Higgs, Phys. Rev. **145**, 1156 (1966).

[8] T. Kibble, Phys. Rev. **155**, 1554 (1967).

[9] ATLAS Collaboration, CERN-PH-EP-2014-122 (2014), submitted to Phys. Rev. D., arXiv:1406.3827 [hep-ex].

[10] CMS Collaboration, CMS-PAS-HIG-14-009 (2014), http://cdsweb.cern.ch/record/1728249.

[11] ATLAS Collaboration, Phys. Lett. B **726**, 120 (2013), arXiv:1307.1432 [hep-ex].

[12] CMS Collaboration, Phys. Rev. Lett. **110**, 081803 (2013), arXiv:1212.6639 [hep-ex].

[13] ATLAS Collaboration, Phys. Lett. B **726**, 88 (2013), arXiv:1307.1427 [hep-ex].

[14] CMS Collaboration, CERN-PH-EP-2014-117 (2014), submitted to Eur. Phys. J. C, arXiv:1407.0558 [hep-ex].

[15] ATLAS Collaboration, CERN-PH-EP-2014-153 (2014), submitted to Eur. Phys. J. C, arXiv:1407.5063 [hep-ex].

[16] ATLAS Collaboration, JINST **3**, S08003 (2008).

[17] ATLAS Collaboration, ATLAS-CONF-2012-048 (2012), http://cdsweb.cern.ch/record/1450089.

[18] ATLAS Collaboration, ATL-PHYS-PUB-2012-003 (2012), http://cdsweb.cern.ch/record/1474107.

[19] T. Sjöstrand, S. Mrenna, P. Skands, Comput. Phys. Commun. **178**, 852 (2008), arXiv:0710.3820 [hep-ph].

[20] S. Heinemeyer *et al.* (LHC Higgs Cross Section Working Group), (2013), 10.5170/CERN-2013-004, arXiv:1307.1347 [hep-ph].

[21] P. Nason, J. High Energy Phys. , 040 (2004), arXiv:hep-ph/0409146 [hep-ph].

[22] S. Frixione, P. Nason, and C. Oleari, J. High Energy Phys. , 070 (2007), arXiv:0709.2092 [hep-ph].

[23] S. Alioli, P. Nason, C. Oleari, and E. Re, J. High Energy Phys. , 043 (2010), arXiv:1002.2581 [hep-ph].

[24] S. Alioli, P. Nason, C. Oleari and E. Re, J. High Energy Phys. , 002 (2009), arXiv:0812.0578 [hep-ph].

[25] E. Bagnaschi, G. Degrassi, P. Slavich, and A. Vicini, J. High Energy Phys. , 088 (2012), arXiv:1111.2854 [hep-ph].

[26] A. Djouadi, M. Spira, and P. Zerwas, Phys. Lett. B **264**, 440 (1991).

[27] S. Dawson, Nucl. Phys. B **359**, 283 (1991).

[28] M. Spira, A. Djouadi, D. Graudenz, and P. Zerwas, Nucl. Phys. B **453**, 17 (1995), arXiv:hep-ph/9504378 [hep-ph].

[29] R. V. Harlander and W. B. Kilgore, Phys. Rev. Lett. **88**, 201801 (2002), arXiv:hep-ph/0201206 [hep-ph].

[30] C. Anastasiou and K. Melnikov, Nucl. Phys. B **646**, 220 (2002), arXiv:hep-ph/0207004 [hep-ph].

[31] V. Ravindran, J. Smith, and W. L. van Neerven, Nucl. Phys. **665**, 325 (2003), arXiv:hep-ph/0302135 [hep-ph].

[32] U. Aglietti, R. Bonciani, G. Degrassi, and A. Vicini, Phys. Lett. B **595**, 432 (2004), arXiv:hep-ph/0404071 [hep-ph].

[33] S. Actis, G. Passarino, C. Sturm, and S. Uccirati, Phys. Lett. B **670**, 12 (2008), arXiv:0809.1301 [hep-ph].

[34] L. Dixon, Y. Li, and S. Hoeche, Private Communication.

[35] L. J. Dixon and M. S. Siu, Phys. Rev. Lett. **90**, 252001 (2003), arXiv:hep-ph/0302233 [hep-ph].

[36] L. J. Dixon and Y. Li, Phys. Rev. Lett. **111**, 111802 (2013), arXiv:1305.3854 [hep-ph].

[37] P. Nason and C. Oleari, J. High Energy Phys. , 037 (2010), arXiv:0911.5299 [hep-ph].

[38] M. Ciccolini, A. Denner, and S. Dittmaier, Phys. Rev. Lett. **99**, 161803 (2007), arXiv:0707.0381 [hep-ph].

[39] M. Ciccolini, A. Denner, and S. Dittmaier, Phys. Rev. D **77**, 013002 (2008), arXiv:0710.4749 [hep-ph].

[40] K. Arnold *et al.*, Comput. Phys. Commun. **180**, 1661 (2009), arXiv:0811.4559 [hep-ph].

[41] P. Bolzoni, F. Maltoni, S.-O. Moch, and M. Zaro, Phys. Rev. Lett. **105**, 011801 (2010), arXiv:1003.4451 [hep-ph].

[42] O. Brein, A. Djouadi, and R. Harlander, Phys. Lett. B **579**, 149 (2004), arXiv:hep-ph/0307206 [hep-ph].

[43] M. Ciccolini, S. Dittmaier, and M. Krämer, Phys. Rev. D **68**, 073003 (2003), arXiv:hep-ph/0306234 [hep-ph].

[44] G. Bevilacqua *et al.*, Comput.Phys.Commun. **184**, 986 (2013), arXiv:1110.1499 [hep-ph].

[45] W. Beenakker *et al.*, Phys. Rev. Lett. **87**, 201805 (2001), arXiv:hep-ph/0107081 [hep-ph].

[46] W. Beenakker *et al.*, Nucl. Phys. B **653**, 151 (2003), arXiv:hep-ph/0211352 [hep-ph].

[47] S. Dawson, L. Orr, L. Reina, and D. Wackeroth, Phys. Rev. D **67**, 071503 (2003), arXiv:hep-ph/0211438 [hep-ph].

[48] S. Dawson, C. Jackson, L. Orr, L. Reina, and D. Wackeroth, Phys. Rev. D **68**, 034022 (2003), arXiv:hep-ph/0305087 [hep-ph].

[49] F. Maltoni and T. Stelzer, J. High Energy Phys. **02**, 027

(2003), arXiv:hep-ph/0208156 [hep-ph].

[50] F. Maltoni, K. Paul, T. Stelzer, and S. Willenbrock, Phys. Rev. D **64**, 094023 (2001), arXiv:hep-ph/0106293 [hep-ph].

[51] V. Barger, M. McCaskey, and G. Shaughnessy, Phys. Rev. D **81**, 034020 (2010), arXiv:0911.1556 [hep-ph].

[52] M. Farina, C. Grojean, F. Maltoni, E. Salvioni, and A. Thamm, J. High Energy Phys. **05**, 022 (2013), arXiv:1211.3736 [hep-ph].

[53] S. Biswas, E. Gabrielli, and B. Mele, J. High Energy Phys. **01**, 088 (2013), arXiv:1211.0499 [hep-ph].

[54] P. Agrawal, S. Mitra, and A. Shivaji, J. High Energy Phys. **12**, 077 (2013), arXiv:1211.4362 [hep-ph].

[55] J. Alwall *et al.*, J. High Energy Phys. , 079 (2014), arXiv:1405.0301 [hep-ph].

[56] M. Bähr *et al.*, Eur. Phys. J. C **58**, 639 (2008), arXiv:0803.0883 [hep-ph].

[57] A. Djouadi, J. Kalinowski, and M. Spira, Comput. Phys. Commun. **108**, 56 (1998), arXiv:hep-ph/9704448 [hep-ph].

[58] S. Actis, G. Passarino, C. Sturm, and S. Uccirati, Nucl. Phys. B **811**, 182 (2009), arXiv:0809.3667 [hep-ph].

[59] H.-L. Lai *et al.*, Phys. Rev. D **82**, 074024 (2010), arXiv:1007.2241 [hep-ph].

[60] J. Pumplin *et al.*, J. High Energy Phys. **07**, 012 (2002).

[61] D. de Florian, G. Ferrera, M. Grazzini, and D. Tommasini, J. High Energy Phys. **06**, 132 (2012), arXiv:1203.6321 [hep-ph].

[62] M. Grazzini and H. Sargsyan, J. High Energy Phys. **09**, 129 (2013), arXiv:1306.4581 [hep-ph].

[63] R. Boughezal, X. Liu, F. Petriello, F. J. Tackmann, and J. R. Walsh, Phys. Rev. D **89**, 074044 (2014), arXiv:1312.4535 [hep-ph].

[64] J. M. Campbell, R. K. Ellis, and G. Zanderighi, J. High Energy Phys. **10**, 028 (2006), arXiv:hep-ph/0608194 [hep-ph].

[65] M. Ciccolini, A. Denner, and S. Dittmaier, Phys. Rev. Lett. **99**, 161803 (2007), arXiv:0707.0381 [hep-ph].

[66] M. Ciccolini, A. Denner, and S. Dittmaier, Phys. Rev. D **77**, 013002 (2008), arXiv:0710.4749 [hep-ph].

[67] A. Denner, S. Dittmaier, S. Kallweit, and A. Muck, J. High Energy Phys. **03**, 075 (2012), arXiv:1112.5142 [hep-ph].

[68] S. Dawson, C. Jackson, L. Reina, and D. Wackeroth, Phys. Rev. D **69**, 074027 (2004), arXiv:hep-ph/0311067 [hep-ph].

[69] S. Dittmaier, M. Kramer, and M. Spira, Phys. Rev. D **70**, 074010 (2004), arXiv:hep-ph/0309204 [hep-ph].

[70] S. Dawson, C. Jackson, L. Reina, and D. Wackeroth, Mod. Phys. Lett. A **21**, 89 (2006), arXiv:hep-ph/0508293 [hep-ph].

[71] R. V. Harlander and W. B. Kilgore, Phys. Rev. D **68**, 013001 (2003), arXiv:hep-ph/0304035 [hep-ph].

[72] R. Harlander, M. Krämer, and M. Schumacher, CERN-PH-TH/2011-134 (2011), arXiv:1112.3478 [hep-ph].

[73] LHC Higgs Cross Section Working Group, S. Dittmaier, C. Mariotti, G. Passarino, and R. Tanaka (Eds.), CERN-2012-002 (CERN, Geneva, 2012), arXiv:1201.3084 [hep-ph].

[74] T. Gleisberg *et al.*, J. High Energy Phys. **02**, 007 (2009), arXiv:0811.4622 [hep-ph].

[75] S. Hoeche, S. Schumann, and F. Siegert, Phys. Rev. D **81**, 034026 (2010), arXiv:0912.3501 [hep-ph].

[76] ATLAS Collaboration, Eur. Phys. J. C **70**, 823 (2010),

arXiv:1005.4568 [physics.ins-det].

[77] S. Agostinelli *et al.* (GEANT4), Nucl. Instrum. Methods A **506**, 250 (2003).

[78] ATLAS Collaboration, ATL-PHYS-PUB-2011-007 (2011), http://cdsweb.cern.ch/record/1345329.

[79] A. Hoecker, P. Speckmayer, J. Stelzer, J. Therhaag, E. von Toerne, and H. Voss, PoS **ACAT**, 040 (2007), arXiv:physics/0703039.

[80] ATLAS Collaboration, ATLAS-CONF-2012-123 (2012), http://cdsweb.cern.ch/record/1473426.

[81] W. Lampl, S. Laplace, D. Lelas, P. Loch, H. Ma, S. Menke, S. Rajagopalan, D. Rousseau, S. Snyder, and G. Unal, ATL-LARG-PUB-2008-002 (2008), http://cdsweb.cern.ch/record/1099735.

[82] M. Cacciari, G. P. Salam, and S. Sapeta, J. High Energy Phys. **04**, 065 (2010).

[83] ATLAS Collaboration, Phys. Rev. D **83**, 052005 (2011), arXiv:1012.4389 [hep-ex].

[84] ATLAS Collaboration, ATLAS-CONF-2010-069 (2010), http://cdsweb.cern.ch/record/1281344.

[85] ATLAS Collaboration, ATLAS-CONF-2014-032 (2014), http://cdsweb.cern.ch/record/1706245.

[86] ATLAS Collaboration, Eur. Phys. J. C **74**, 2941 (2014), arXiv:1404.2240 [hep-ex].

[87] ATLAS Collaboration, CERN-PH-EP-2014-151 (2014), arXiv:1407.3935 [hep-ex].

[88] M. Cacciari, G. P. Salam, and G. Soyez, J. High Energy Phys. **04**, 063 (2008), arXiv:0802.1189 [hep-ph].

[89] ATLAS Collaboration, CERN-PH-EP-2013-222 (2014), arXiv:1406.0076 [hep-ex].

[90] M. Cacciari and G. P. Salam, Phys. Lett. B **659**, 119 (2008), arXiv:0707.1378 [hep-ph].

[91] ATLAS Collaboration, ATLAS-CONF-2013-083 (2013), http://cdsweb.cern.ch/record/1570994.

[92] ATLAS Collaboration, ATLAS-CONF-2011-102 (2011), http://cdsweb.cern.ch/record/1369219.

[93] ATLAS Collaboration (ATLAS), ATLAS-CONF-2014-046 (2014), http://cdsweb.cern.ch/record/1741020.

[94] ATLAS Collaboration, ATLAS-CONF-2013-082 (2013), http://cdsweb.cern.ch/record/1570993.

[95] ATLAS Collaboration, ATLAS-CONF-2012-101 (2012), http://cdsweb.cern.ch/record/1463915.

[96] ATLAS Collaboration, to be submitted to Phys. Lett. B. (2014).

[97] The quantity p_{Tt} is defined as $p_{\mathrm{Tt}} = |(\vec{p}_{\mathrm{T}}^{\gamma 1} + \vec{p}_{\mathrm{T}}^{\gamma 2}) \times \hat{\mathbf{t}}|$, where $\hat{\mathbf{t}} = (\vec{p}_{\mathrm{T}}^{\gamma 1} - \vec{p}_{\mathrm{T}}^{\gamma 2})/|\vec{p}_{\mathrm{T}}^{\gamma 1} - \vec{p}_{\mathrm{T}}^{\gamma 2}|$ denotes the thrust axis in the transverse plane, and $\vec{p}_{\mathrm{T}}^{\gamma 1}$, $\vec{p}_{\mathrm{T}}^{\gamma 2}$ are the transverse momenta of two photons γ_1 and γ_2.

[98] D. Rainwater, R. Szalapski, and D. Zeppenfeld, Phys. Rev. D **54**, 6680 (1996), arXiv:hep-ph/9605444.

[99] M. Oreglia, SLAC-R-0236 , Appendix D (1980).

[100] ATLAS Collaboration, Phys. Rev. D **85**, 012003 (2012), arXiv:1107.0581 [hep-ex].

[101] ATLAS Collaboration, J. High Energy Phys. **01**, 086 (2013), arXiv:1211.1913 [hep-ex].

[102] G. Cowan, K. Cranmer, E. Gross, and O. Vitells, European Physical Journal C **71**, 1554 (2011), arXiv:1007.1727 [physics.data-an].

[103] S. N. Bernstein, Comm. Soc. Math. Kharkov **13**, 1 (1912).

[104] ATLAS Collaboration, Eur. Phys. J. C **73**, 2518 (2013), arXiv:1302.4393 [hep-ex].

[105] ATLAS Collaboration, Eur. Phys. J. C **72**, 1849 (2012),

arXiv:1110.1530 [hep-ex].

[106] I. W. Stewart and F. J. Tackmann, Phys. Rev. D **85**, 034011 (2012), arXiv:1107.2117 [hep-ph].

[107] S. Gangal and F. J. Tackmann, Phys. Rev. D **87**, 093008 (2013), arXiv:1302.5437 [hep-ph].

[108] J. M. Campbell, R. K. Ellis, and C. Williams, Phys. Rev. D **81**, 074023 (2010), arXiv:1001.4495 [hep-ph].

[109] ATLAS Collaboration, ATLAS-CONF-2010-053 (2010), http://cdsweb.cern.ch/record/1281310.

[110] ATLAS Collaboration, Phys. Rev. D **86**, 032003 (2012), arXiv:1207.0319 [hep-ex].

[111] M. H. Quenouille, Journal of the Royal Statistical Society. Series B (Methodological) **11**, 68 (1949).

[112] J. W. Tukey, Annals of Math. Statist. 29 (1958) 614.

[113] ATLAS Collaboration, CERN-PH-EP-2014-148 (2014), submitted to J. High Energy Phys., arXiv:1407.4222 [hep-ex].